



An approximate technique to test chaotic region in a rotating pendulum system with bistable characteristics

Ning Han · Peipei Lu · Zhixin Li

Received: 15 June 2020 / Accepted: 1 February 2021

© The Author(s), under exclusive licence to Springer Nature B.V. part of Springer Nature 2021

Abstract This paper is concerned with the chaotic dynamics of a rotating pendulum system with bistable characteristics subjected to a viscous damping and a harmonic forcing. As a prototype of the single-degree-of-freedom system with bistable characteristics, this pendulum system exhibits a transition from smooth to discontinuous dynamics by changing a geometrical parameter. The dynamic behaviors of the unperturbed system with irrational nonlinearity bear significant similarities to the coupling of a simple pendulum and the smooth and discontinuous (SD) oscillator with the coexistence of the standard homoclinic orbits of Duffing type and pendulum type and the coexistence of the nonstandard homoclinic orbits of SD type and pendulum type in the smooth and discontinuous case, respectively. For the perturbed smooth system, we present an approximate technique to analytically obtain the lower bound line for horseshoes chaos arising from the homoclinic orbits of Duffing-type and Pendulum-type tangling, which overcomes the natural difficulties of solving the analytical expression of the homoclinic orbits and calculating the complicated Melnikov inte-

grals. The chaotic thresholds of the perturbed discontinuous system are calculated by applying the numerical technique due to its non-smooth feature. Numerical simulations are carried out to certify the chaotic thresholds, which show the efficiency of the proposed techniques and demonstrate the predicated chaotic motions. Finally, different types of chaotic motions are illustrated via the cylindrical phase portraits. The contribution of this study is also helpful for exploring the dynamical behaviors of the complex nonlinear dynamical system containing the standard homoclinic or heteroclinic orbit in terms of the quantitative calculation.

Keywords Rotating pendulum · Bistable characteristics · Melnikov method · Chaotic threshold · Irrational nonlinearity

1 Introduction

Pendulum [1–3] is a simple system that is usually related to great discoveries in engineering applications [4], artificial intelligence [5], scientific education [6], medicine [7], etc. In particular, an explosion of pendulum studies has produced a flood of information on nonlinear dynamics in term of oscillations [8–10], rotations [11–13], bifurcations [14–16], chaos [17–19], synchronization [20–22], experimental investigation [23–26], energy absorption [27–29], etc. This paper reports a classical pendulum system with bistable characteristics [30], which possesses a cylindrical transitions from

N. Han (✉) · P. Lu
Key Lab. of Machine Learning and Computational Intelligence, College of Mathematics and Information Science, Hebei University, Baoding 071002, China
e-mail: ninghan@hbu.edu.cn

Z. Li
College of Mathematical Science and Engineering, Hebei University of Engineering, Handan 056038, China
e-mail: lzxin1234@163.com

smooth to discontinuous double well dynamics via changing a geometrical parameter. Interestingly, this rotating pendulum system has successfully combined the bistable and non-smooth characteristics with simple pendulum.

With the discovery of chaos [31,32] and the advent of computers, the chaotic dynamics of nonlinear dynamical system has become a hot topic in recent decades [33,34], which especially set off a new round of upsurge of the study of pendulum. In particular, Melnikov method [35] has been greatly developed as an analytical method to argue the existence of classical chaos in one-dimensional nonlinear dynamical system subjected to small time-periodic perturbation. Smooth and non-smooth chaos prediction using the Melnikov method has been widely described as a topical subject [36]. Notice that the key ingredient in Melnikov method is based upon investigating generalized integrals along homoclinic or heteroclinic orbits to normally hyperbolic invariant manifolds. In general, two age-old natural problems with such approach are how to solve the analytical expression of the singular closed trajectory and calculate the corresponding generalized Melnikov integrals. In most real-life systems, such analytical expression of the homoclinics or heteroclinic orbits and the corresponding Melnikov integrals, however, would not be expressed through simple formulas. In other words, very few nonlinear dynamical systems can be solved analytically such as Duffing oscillator [37,38], simple pendulum [39], inverted pendulum and pendulum-like system [40] etc.

To solve such natural problems, many techniques have been developed to detect the chaotic thresholds for the complicated nonlinear dynamical system based upon Melnikov method. In 2006, Awrejcewicz et al. analytically predicted homoclinic bifurcation in a class of double self-excited Duffing-type oscillator by means of Melnikov–Gruender approach and the predicted stick-slip chaotic motion can be verified by numerical simulations [41]. In 2008, Cao et al. introduced a triple linear approximation [42] to semi-analytically calculate the homoclinic tangling of an archetypal smooth and discontinuous (SD) oscillator [43] subjected to damping and driving with the help of Melnikov method. In 2009, Zhang et al. calculated the analytical prediction of multi-pulse chaotic motion for the nonlinear non-planar oscillations of a cantilever beam by means of the extended Melnikov method [44]. In 2012, Han et al. utilized Taylor’s expansion technique to obtain

the analytical criteria of chaos arising from different kinds of singular closed orbits tangling in the coupled smooth and discontinuous oscillator [45]. Based upon an extended Pade approximation, Feng et al. made a Melnikov analysis to investigate the chaotic dynamics for a classes of multi-stable dynamical systems with asymmetric potentials under the perturbations of external and parametric excitation [46]. To avoid Taylor’s expansion and retain natural characteristics, in 2014, Tian et al. developed an effective extended Melnikov method to derive the chaotic boundary of a spring–pendulum system having a complicated nonlinear restoring force with irrational and fractional terms [47]. In 2018, Zhang et al. [48] studied the chaotic behaviors of a nanoplate postulating nonlinear Winkler foundation, which can be described to Duffing equation whose chaotic thresholds is examined analytically by using Melnikov method. Recently, Ren et al. have derived the possible parameter area that triggers chaotic motion in the flexible shaft rotating–lifting system [49] by means of Melnikov method. This work resolves these two natural problems in a different way: an effective technique is proposed to semi-analytically obtain the chaotic thresholds corresponding to the homoclinic orbits of Duffing type and pendulum type in a rotating pendulum system with bistable characteristics, which overcome the natural difficulties of solving the analytical expression of the singular closed trajectory and calculating the complicated generalized integrals in applying Melnikov method. It is concluded that this approximate technique can be widely used to study the threshold of Horseshoes chaos in complex dynamical systems with standard homoclinic or heteroclinic orbits.

In fact, the headline funding of this study is to present an effective technique to analyze the horseshoes chaos arising from the standard homoclinic or heteroclinic orbits tangling in low-dimensional nonlinear dynamical system subjected to small time-periodic perturbation. To this end, this paper can be organized as follows. In Sect. 2, the equation of motion for a rotating pendulum system with bistable characteristics subjected to both the viscous damping and external harmonic forcing is derived. In Sect. 3, the phase trajectories of unperturbed system can be studied by means of the Hamiltonian function; in particular, the coexistence of the standard homoclinic orbits of Duffing type and pendulum type and the coexistence of the nonstandard homoclinic orbits of SD type and pendulum type are reported in the smooth and discontinuous case. In Sect. 4, an effective

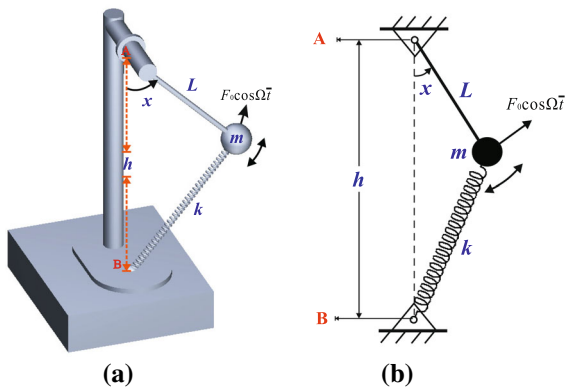


Fig. 1 (Color online) Model of the rotating pendulum with bistable characteristics: **a** mechanical model and corresponding simplified plane model **(b)**

technique is proposed to calculate the chaotic criteria resulted in homoclinic tangling in the rotating pendulum system by means of the Melnikov method, and then, the numerical simulations are utilized to verify the efficiency of the criteria. Finally we summarize the conclusions and provide the further challenge in Sect. 5.

2 Equation of motion

A rotating mechanical model is illustrated in Fig. 1a, which is regard as the coupling of simple pendulum and spring–mass oscillator. For a better understanding of geometrical structure of mechanical model, the corresponding simplified plane model is constructed in Fig. 1b.

Consider the rotating mechanical model subjected to a viscous damping (with coefficient C related to linear velocity) as well as an external harmonic forcing (with amplitude F_0 and frequency Ω) in the direction of motion, and then, the differential equation can be expressed as

$$mLx'' + CLx' + mg \sin x + kh \sin x \left(1 - \frac{l}{\sqrt{L^2 + h^2 - 2hL \cos x}} \right) = F_0 \cos \Omega \bar{t}, \tag{1}$$

where the prime denotes derivative with respect to time \bar{t} , x represents the angular displacement of motion, m corresponds to the quality of the lump mass, L is the length of massless rod, l and k are the free length and

stiffness of spring, h represents the distance between the point **A** and point **B**, always assumed $h \geq L$ and g is the gravitational constant, respectively.

Introducing non-dimensional time $t = \sqrt{g/L} \bar{t}$ and defining $L = l$, a dimensionless form of this rotating pendulum system (1) is given by

$$\ddot{x} + \xi \dot{x} + \sin x + q\lambda \sin x \left(1 - \frac{1}{\sqrt{1 + \lambda^2 - 2\lambda \cos x}} \right) = f_0 \cos \omega t, \tag{2}$$

where

$$\xi = \frac{C}{m} \sqrt{\frac{L}{g}}, \quad \omega_p = \sqrt{\frac{g}{L}}, \quad \omega_s = \sqrt{\frac{k}{m}},$$

$$q = \frac{\omega_s^2}{\omega_p^2}, \quad \lambda = \frac{h}{L}, \quad f_0 = \frac{F_0}{mg}, \quad \omega = \sqrt{\frac{L}{g}} \Omega.$$

Note that the dot denotes derivative with respect to t in system (2). One systemic parameter q represents the ratio of natural frequency between spring–mass oscillator and simple pendulum, and the other systemic parameter λ reflects the geometrical structure of the proposed model, respectively. Note that a transition from the smooth dynamics to the discontinuous dynamics occurs on system (2) by decreasing the smoothness parameter λ to 1 from a mathematical point of view.

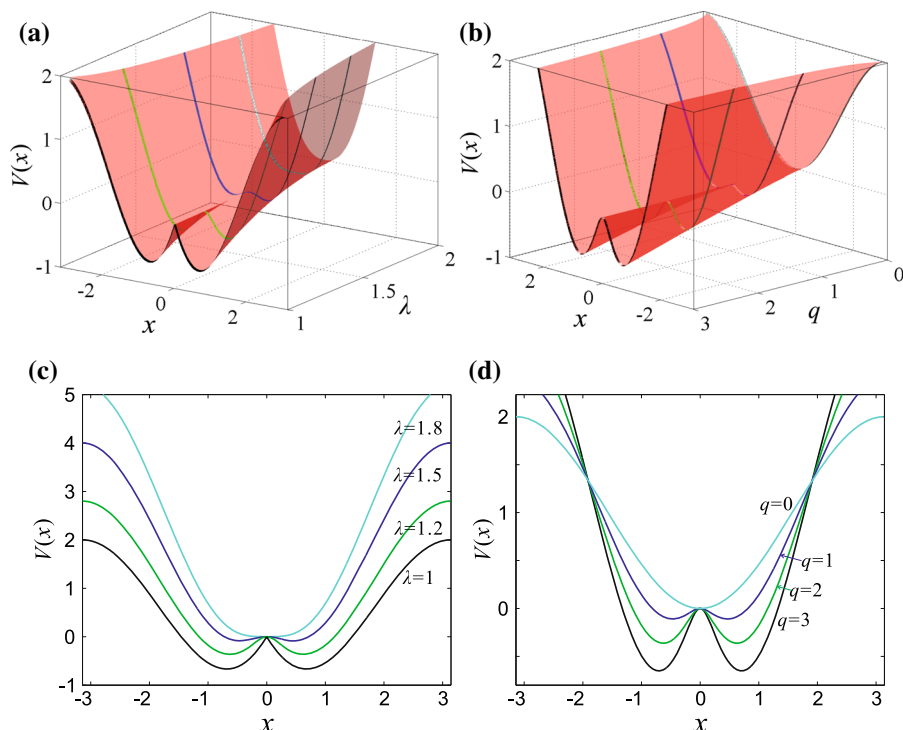
3 Standard and nonstandard homoclinic orbits

In this section, the phase trajectories of unperturbed system can be studied with the help of the Hamiltonian; in particular, the coexistence of the standard homoclinic orbits of Duffing type and pendulum type and the coexistence of the nonstandard homoclinic orbits of SD type and pendulum type are reported in the smooth and discontinuous case.

When $f_0 = 0$ and $\xi = 0$, the unperturbed system of the rotating pendulum (2) can be written as a two-dimensional one

$$\begin{cases} \dot{x} = y, \\ \dot{y} = -\sin x - q\lambda \sin x \left(1 - \frac{1}{\sqrt{1 + \lambda^2 - 2\lambda \cos x}} \right). \end{cases} \tag{3}$$

Fig. 2 (Color online) **a** Potential surface of unperturbed system (3) in the $x\lambda V$ plane for $q = 2$, **b** potential surface in the xqV plane for $\lambda = 1.2$. **c** Effect of parameter λ on potential curves, **d** effect of parameter q on potential curves



Note that we define $x \in [-\pi, \pi]$ due to its periodicity. Letting $\dot{x} = 0$ and $\dot{y} = 0$, the equilibria of system (3) can be expressed as

$$\begin{aligned} (x_1, y_1) &= (0, 0), \quad (x_{2,3}, y_{2,3}) \\ &= (\pm\pi, 0), \quad (x_{4,5}, y_{4,5}) \end{aligned} \tag{4}$$

$$= (\pm \arccos \rho, 0), \quad \rho = \frac{1 + \lambda^2}{2\lambda} - \frac{q^2\lambda}{2(1 + q\lambda)^2},$$

when $|\rho| < 1$. According to the eigenvalues at equilibria (x_i, y_i) , we found that the conservative system (3) possesses three saddle points $(x_{1,2,3}, y_{1,2,3})$ and two centers $(x_{4,5}, y_{4,5})$. The detailed analysis is shown in Appendix (a) and (b) for $\xi = 0$.

In order to clarify the origin of non-smoothness in the conservative system (3), especially the effects of parameters λ and q on potential energy $V(x)$ of the conservative system (3),

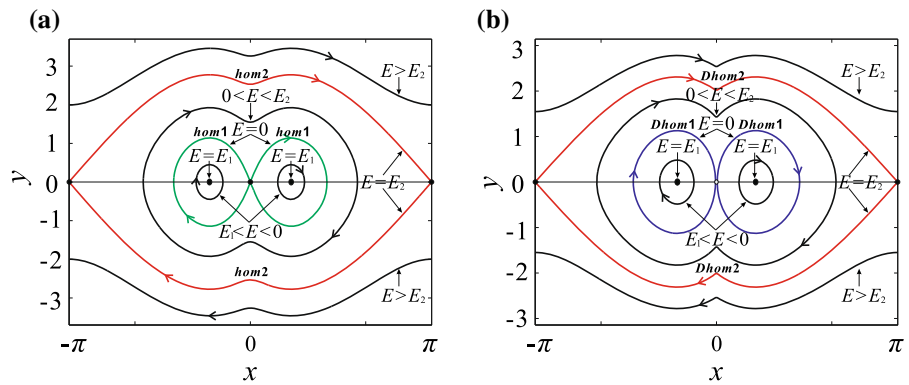
$$V(x) = -(1 + q\lambda) \cos x - q\sqrt{1 + \lambda^2 - 2\lambda \cos x} + 2q\lambda - q + 1, \tag{5}$$

the potential energy is plotted in Fig. 2. For the convenience of analysis, we always assume that the value of potential energy is zero for $x = 0$ in Eq. (5). When $q = 2$, Fig. 2a shows a potential surface in the $x\lambda V$ -plane which means that the conservative system (3) bears a transitions from single potential well to double potential well by decreasing parameter λ . In particular, for $\lambda = 1$, the potential energy $V(x)$ of non-smooth system can be written as

$$V(x) = -(1 + q) \cos x - 2q \left| \sin \frac{x}{2} \right| + q + 1. \tag{6}$$

Clearly, the derivative of $V(x)$ at $x = 0$ suddenly switches from zero to nonexistence due to the absolute value function when parameter λ is reduced to one. To further explore the effect of parameter λ on the potential curves, especially non-smoothness, the potential curves are plotted for different values of parameter λ in Fig. 2c. When $\lambda = 1.2$, Fig. 2b displays a potential surface in the xqV -plane. It is found that system exhibits a transitions from single potential well to double potential well as parameter q increases; the details are shown in Fig. 2d.

Fig. 3 (Color online) **a** Phase portraits of smooth case with the coexistence of the homoclinic orbits of Duffing type (*hom1*) and pendulum type (*hom2*) for $q = 3, \lambda = 1.2$, **b** phase portraits of discontinuous case with the coexistence of the nonstandard homoclinic orbit of SD type (*Dhom1*) and the pendulum type (*Dhom2*) for $q = 2, \lambda = 1$



Then we can derive the Hamiltonian function which written as follows

$$H(x, y) = \frac{y^2}{2} - (1 + q\lambda) \cos x - q\sqrt{1 + \lambda^2 - 2\lambda \cos x} + 2q\lambda - q + 1. \tag{7}$$

With the help of the Hamiltonian function (7), for $H(x, y) = E$, the representative phase trajectories of system (3) are plotted for the chosen parameters q and λ in Fig. 3. This system exhibits similar behavior of the double well dynamics with the coexistence of the homoclinic orbits of Duffing type and pendulum type marked by *hom1* and *hom2*, as shown in Fig. 3a. From a mathematical standpoint, we can transform the smooth system into non-smooth system with the nonstandard homoclinic orbits of SD type [43] (*Dhom1*) and pendulum type (*Dhom2*) by diminishing the geometrical parameter λ to 1. Similarly, the nonstandard homoclinic orbits of SD type (blue) connecting a saddle-like point (0, 0) and the nonstandard homoclinic orbits of pendulum type (red) connecting two saddle point ($\pm\pi, 0$) are coexistence and depicted in Fig. 3b.

Assuming $f_0 = 0$ and $\omega = 0$, the dynamic behaviors of the weak damping pendulum system can be investigated by means of equilibrium analysis, phase portraits and attractive basin. To explore the effect of dissipative term ξ on five equilibria (x_i, y_i) , the Jacobian matrix and the corresponding characteristic equations are introduced in dissipative system with bistable characteristics, as shown in Appendix. When the dissipative term ξ is sufficiently small, we conclude that $(x_{1,2,3}, y_{1,2,3})$ are saddle points with two unequal real eigenvalues and $(x_{4,5}, y_{4,5})$ represent a pair of sta-

ble focuses with conjugate virtual eigenvalues. Due to the existence of positive dissipative term ξ , the closed phase trajectories in Fig. 3 will break and then tend to stable equilibria $(x_{4,5}, y_{4,5})$ in the form of inward spiral, as shown in Fig. 4. Figure 4 shows the attractive basins of two stable equilibria $(x_{4,5}, y_{4,5})$ and the corresponding perturbed manifolds over a period $x \in [-\pi, \pi]$. Note that the stable manifolds correspond to the boundaries of two attractive basin denoted by the gray region and the dark region. Figure 4a depicts the damped behavior of the smooth case, where the stable manifolds denoted by S get infinitely close to the saddle points and the unstable manifolds marked by U is away from the saddle points and then flows indefinitely into the stable equilibria $(x_{4,5}, y_{4,5})$. Similarly, the damped behavior of the discontinuous case is plotted in Fig. 4b. The details of all parameters taken in Fig. 4 can be found in the corresponding captions.

4 Chaotic dynamics

Smooth and non-smooth chaos prediction using the Melnikov method has been widely described as a topical subject [36,39]. In this section, Melnikov method is employed to obtain the chaotic thresholds for the coexistence of the standard homoclinic orbits of Duffing type and pendulum type and the coexistence of the non-standard homoclinic orbits of SD type and pendulum type in smooth and discontinuous cases, respectively.

Then we will give the detailed process of Melnikov analysis for the perturbed system (2), the expository discussions of theory are seen in [35]. Moreover, we introduce the following notation in system (2):

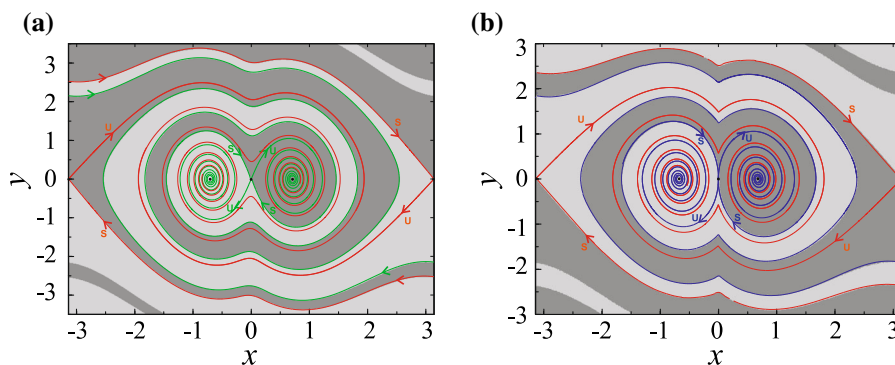


Fig. 4 (Color online) Damped behavior of the pendulum system (2) for $f_0 = 0, \omega = 0$ and $\xi = 0.2$, **a** attractive basin of the smooth case for $q = 3$ and $\lambda = 1.2$, **b** attractive basin of

the discontinuous case for $q = 2$ and $\lambda = 1$, respectively (the dark region represents the attractive basin of point (x_4, y_5) and the gray region denotes the attractive basin of point (x_5, y_5))

$$X = \begin{pmatrix} x \\ y \end{pmatrix}, \quad F(X) = \begin{pmatrix} y \\ F(x) \end{pmatrix},$$

$$G(X, t) = \begin{pmatrix} 0 \\ -\xi y + f_0 \cos \omega t \end{pmatrix},$$

where

$$F(X(t)) \wedge G(X(t), t + \tau) = -\xi y^2(t) + y(t) f_0 \cos \omega(t + \tau),$$

where $a \wedge b = a_1 b_2 - a_2 b_1$, for any $a = (a_1, a_2)^T$ and $b = (b_1, b_2)^T$, and the corresponding Melnikov function [35, 39, 42] of system is given by

$$M(\tau) = -\xi \int_{-\infty}^{+\infty} y^2(t) dt + f_0 \int_{-\infty}^{+\infty} y(t) \cos \omega(t + \tau) dt. \quad (8)$$

The Melnikov function $M(\tau) = 0$ has zero roots for τ , which indicates that the stable and unstable manifolds will intersect each other. Once the stable and unstable manifolds intersect transversely, they will intersect an infinite number of times. The phase space will have rapid expansion and contraction which will eventually lead to horseshoe dynamics [39].

4.1 Melnikov analysis for the smooth system

Note that the dynamic behaviors of the unperturbed smooth system (3) with irrational nonlinearity are similar to simple pendulum coupled with SD oscillator with the coexistence of the homoclinic orbits of Duffing type and pendulum type in Sect. 3. Since the analytical expressions for the homoclinic orbits of Duffing type

and pendulum type cannot be expressed through simple formulas due to its strongly irrational nonlinearity, two approximate analytical solutions can be defined by means of the mathematical characteristics of the homoclinic orbits to analytically calculate the Melnikov integrals.

The homoclinic orbits of Duffing type (*hom1*) connecting a standard saddle point $(0, 0)$ is plotted with green in Fig. 5a, of which the main mathematical features satisfy

$$\lim_{t \rightarrow +\infty} x_{\Gamma_{1,2}}^{hom1}(t) = 0,$$

$$\lim_{t \rightarrow -\infty} x_{\Gamma_{1,2}}^{hom1}(t) = 0. \quad (9)$$

Based upon the mathematical features and the analytical expression of conventional homoclinic orbits [39], the approximate analytical solution of the homoclinic orbits of Duffing type can be defined as

$$\begin{aligned} (x_{\Gamma_{1,2}}^{hom1}(t), y_{\Gamma_{1,2}}^{hom1}(t)) = & \left(\mp A_1 \cot^{-1} (B_1 \cosh (C_1 t)), \right. \\ & \left. \pm \frac{A_1 B_1 C_1 \sinh (C_1 t)}{1 + B_1^2 \cosh^2 (C_1 t)} \right), \end{aligned} \quad (10)$$

where $t \in (-\infty, +\infty)$ and $A_1 > 0, B_1 > 0, C_1 > 0$. Note that the details of the homoclinic orbits of pendulum type (*hom2*) colored in red are described in Fig. 5a, of which the main mathematical features satisfy

$$\lim_{t \rightarrow +\infty} x_{\Gamma_{1,2}}^{hom2}(t) = \pm \pi,$$

$$\lim_{t \rightarrow -\infty} x_{\Gamma_{1,2}}^{hom2}(t) = \mp \pi. \quad (11)$$

Fig. 5 (Color online) **a** Details of the standard homoclinic orbits of Duffing type (*hom1*) and pendulum type (*hom2*) for the smooth system, **b** details of the nonstandard homoclinic orbits of SD type (*Dhom1*) and pendulum type (*Dhom2*) for the discontinuous system

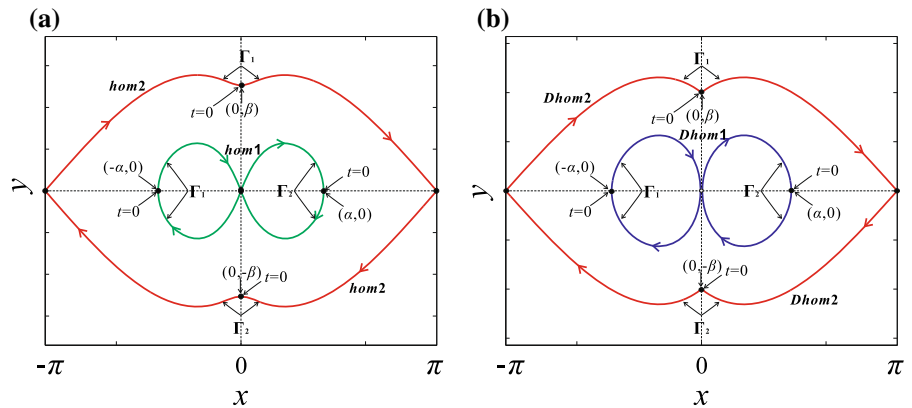
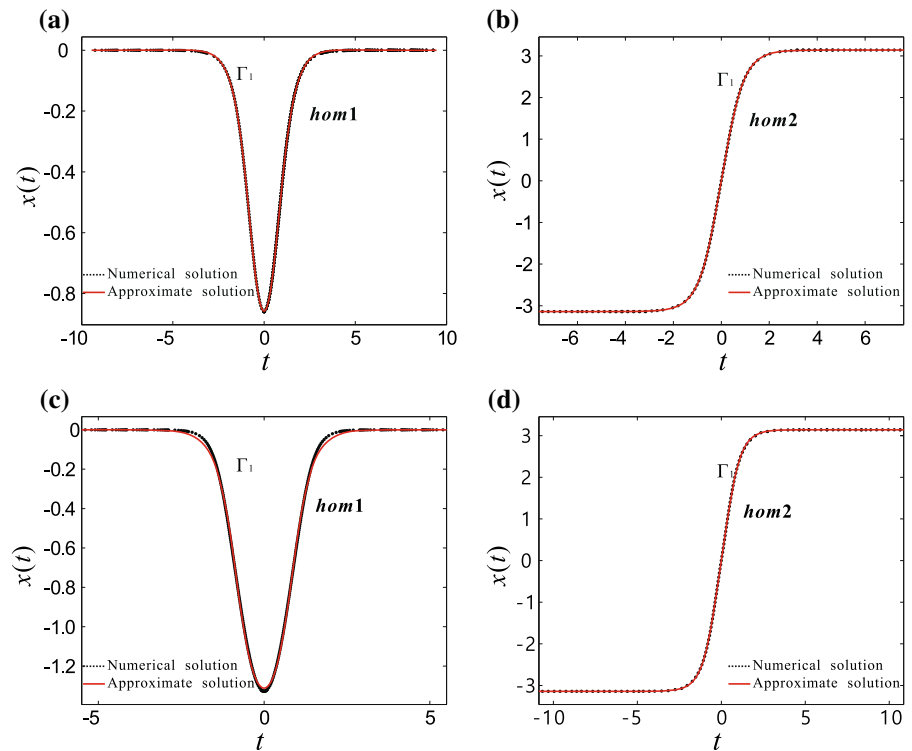


Fig. 6 (Color online) Comparisons between the numerical solution marked by the black dotted lines and the approximate analytical solution marked by the red solid lines, **a** and **c** homoclinic orbits of Duffing type for $q = 3, \lambda = 1.5$ and $q = 3, \lambda = 1.2$, **b** and **d** homoclinic orbits of pendulum type for $q = 3, \lambda = 1.5$ and $q = 3, \lambda = 1.2$, respectively



Similarly, the approximate analytical solutions of the homoclinic orbits of pendulum type connecting two standard saddle points $(-\pi, 0)$ and $(\pi, 0)$ can be defined as

$$\left(x_{\Gamma_{1,2}}^{hom2}(t), y_{\Gamma_{1,2}}^{hom2}(t) \right) = \left(\pm A_2 \tan^{-1} (B_2 \sinh (C_2 t)), \pm \frac{A_2 B_2 C_2 \cosh (C_2 t)}{1 + B_2^2 \sinh^2 (C_2 t)} \right), \quad (12)$$

where $t \in (-\infty, +\infty)$ and $A_2 > 0, 1 > B_2 > 0, C_2 > 0$.

Then, we begin to calculate the Melnikov integrals corresponding to the homoclinic orbits of Duffing type and pendulum type based upon the approximate analytical solutions. It is worth pointing out that $y_{\Gamma_{1,2}}^{hom1}(t)$ are odd function in Eq. (10), and then, the Melnikov function (8) for the homoclinic orbits of Duffing type denoted by green in Fig. 5a can be expressed as

$$M_{hom1}(\tau) = -\xi \int_{-\infty}^{+\infty} (y_{\Gamma_{1,2}}^{hom1}(t))^2 dt - f_0 \sin \omega \tau \int_{-\infty}^{+\infty} y_{\Gamma_{1,2}}^{hom1}(t) \sin \omega t dt. \quad (13)$$

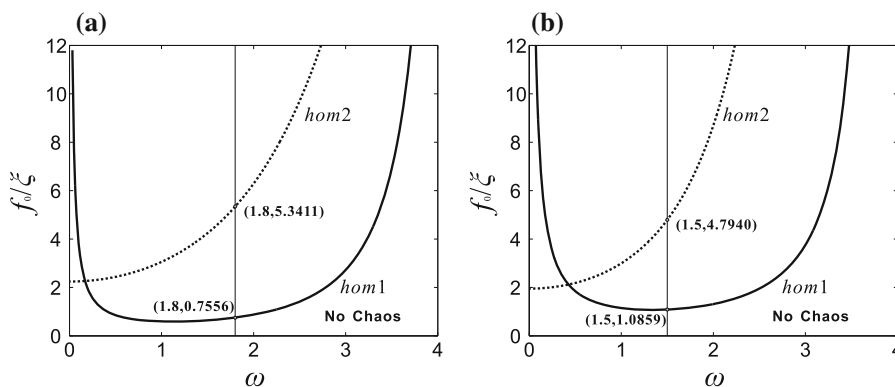


Fig. 7 Chaotic thresholds of the homoclinic orbits of Duffing type denoted by the solid line ($f_0/\xi = R_{hom1}(\omega)$) and the homoclinic orbits of pendulum type denoted by the dashed line

($f_0/\xi = R_{hom2}(\omega)$) for **a** $q = 3, \lambda = 1.5, R_{hom1}(1.8) = 0.7556, R_{hom2}(1.8) = 5.3411$ and **b** $q = 3, \lambda = 1.2, R_{hom1}(1.5) = 1.0859, R_{hom2}(1.5) = 4.7940$, respectively

The Melnikov integrals for the homoclinic orbits of the Duffing type can be derived as

$$\begin{aligned}
 I_1^{hom1} &= \int_{-\infty}^{+\infty} (y_{\Gamma_{1,2}}^{hom1}(t))^2 dt = \int_{-\infty}^{+\infty} \left(\pm \frac{A_1 B_1 C_1 \sinh(C_1 t)}{1 + B_1^2 \cosh^2(C_1 t)} \right)^2 dt \\
 &= A_1^2 C_1 \left(1 - \frac{B_1^2}{2\sqrt{1 + B_1^2}} \ln \left(\frac{2 + B_1^2 + 2\sqrt{1 + B_1^2}}{B_1^2} \right) \right), \tag{14}
 \end{aligned}$$

$$\begin{aligned}
 I_2^{hom1} &= \int_{-\infty}^{+\infty} y_{\Gamma_{1,2}}^{hom1}(t) \sin \omega t dt = \int_{-\infty}^{+\infty} \left(\pm \frac{A_1 B_1 C_1 \sinh(C_1 t)}{1 + B_1^2 \cosh^2(C_1 t)} \right) \sin \omega t dt \\
 &= \pm A_1 \pi \sin \left(\frac{\omega}{C_1} \sinh^{-1} \frac{1}{B_1} \right) \operatorname{sech} \left(\frac{\pi \omega}{2C_1} \right). \tag{15}
 \end{aligned}$$

It is worth reiterating here that $M_{hom1}(\tau) = 0$ has simple zero for τ if and only if the following inequality holds:

$$\frac{f_0}{\xi} > \left| \frac{I_1^{hom1}}{I_2^{hom1}} \right| = R_{hom1}(\omega). \tag{16}$$

Clearly, the approximate analytical solutions $y_{\Gamma_{1,2}}^{hom2}(t)$ are even function in Eq. (12). So the Melnikov function (8) for the homoclinic orbits of pendulum type colored in red in Fig. 5a can be expressed as

$$\begin{aligned}
 M_{hom2}(\tau) &= -\xi \int_{-\infty}^{+\infty} (y_{\Gamma_{1,2}}^{hom2}(t))^2 dt \\
 &\quad + f_0 \cos \omega \tau \int_{-\infty}^{+\infty} y_{\Gamma_{1,2}}^{hom2}(t) \cos \omega t dt. \tag{17}
 \end{aligned}$$

Introducing symbols I_1^{hom2} and I_2^{hom2} , the Melnikov integrals for the homoclinic orbits of the pendulum type can be obtained as

Fig. 8 (Color online) **a** Bifurcation diagram for f_0 versus x with the thresholds $f_0^{hom1} = 0.0456$ marked by the solid line for $q = 3, \lambda = 1.5, \xi = 0.2, \omega = 1.5$, and the corresponding Lyapunov exponents **(b)**. When $q = 3, \lambda = 1.2, \xi = 0.2, \omega = 1.7$, **c** bifurcation diagram for f_0 versus x with the thresholds $f_0^{hom1} = 0.0456$ marked by the solid line, and the corresponding Lyapunov exponents **(d)**. **e** and **f** Two types of chaotic attractors for $f_0 = 0.3$ and 2.3 , **g** and **h** corresponding stable and unstable manifolds

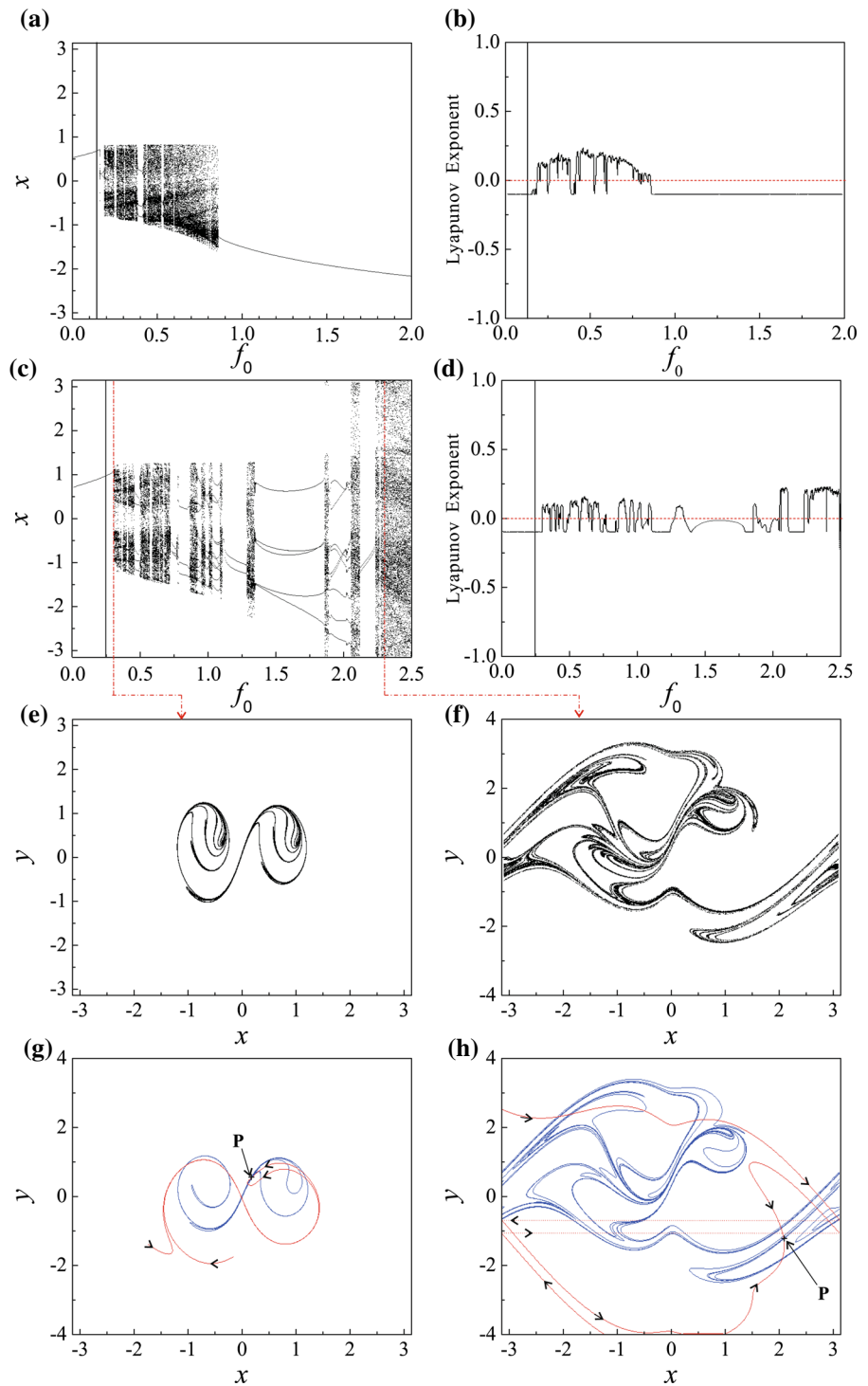
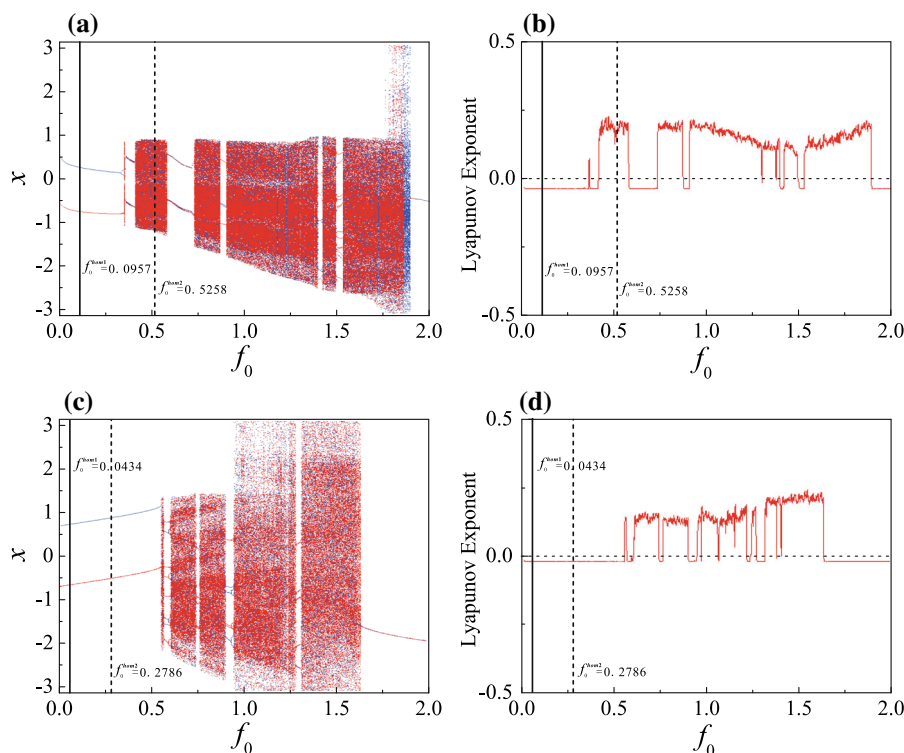


Fig. 9 (Color online) When $q = 3, \lambda = 1.5, \xi = 0.06, \omega = 1.8$, **a** the bifurcation diagram for f_0 versus x with the thresholds $f_0^{hom1} = 0.0456$ marked by the solid line and $f_0^{hom2} = 0.3205$ marked by the dash line, and the corresponding Lyapunov exponents **(b)**. **c** Bifurcation diagram for f_0 versus x with the thresholds $f_0^{hom1} = 0.0434$ marked by the solid line and $f_0^{hom2} = 0.1918$ marked by the dash line at $q = 3, \lambda = 1.2, \xi = 0.04, \omega = 1.5$, **d** the corresponding Lyapunov exponents, respectively



$$\begin{aligned}
 I_1^{hom2} &= \int_{-\infty}^{+\infty} (y_{\Gamma_{1,2}}^{hom2}(t))^2 dt = \int_{-\infty}^{+\infty} \left(\mp \frac{A_2 B_2 C_2 \cosh(C_2 t)}{1 + B_2^2 \sinh^2(C_2 t)} \right)^2 dt; \\
 &= A_2^2 C_2 \left(1 - \frac{B_2^2}{2\sqrt{1 - B_2^2}} \ln \left(\frac{2 - B_2^2 - 2\sqrt{1 - B_2^2}}{B_2^2} \right) \right), \tag{18}
 \end{aligned}$$

$$\begin{aligned}
 I_2^{hom2} &= \int_{-\infty}^{+\infty} y_{\Gamma_{1,2}}^{hom2}(t) \cos \omega t dt = \int_{-\infty}^{+\infty} \left(\mp \frac{A_2 B_2 C_2 \cosh(C_2 t)}{1 + B_2^2 \sinh^2(C_2 t)} \right) \cos \omega t dt \\
 &= \mp A_2 \pi \cos \left(\frac{\omega}{C_2} \sinh^{-1} \sqrt{\frac{1}{B_2^2} - 1} \right) \operatorname{sech} \left(\frac{\pi \omega}{2C_2} \right). \tag{19}
 \end{aligned}$$

Similarly, $M_{hom2}(\tau) = 0$ has simple zero for τ if and only if the following inequality holds:

$$\frac{f_0}{\xi} > \left| \frac{I_1^{hom2}}{I_2^{hom2}} \right| = R_{hom2}(\omega). \tag{20}$$

In order to detect the lower bound line for horseshoes chaos of the perturbed pendulum system (2), we define the function $\bar{R}_s(\omega)$ as follows

$$\bar{R}_s(\omega) = \min\{R_{hom1}(\omega), R_{hom2}(\omega)\}. \tag{21}$$

In fact, no chaotic region can be given for the parameters satisfying $f_0/\xi < \bar{R}_s(\omega)$. On the contrary, the chaotic motion must exist in the region satisfying $f_0/\xi > \bar{R}_s(\omega)$.

Thus, two bistable examples are given to demonstrate the above theoretical results. When $q = 3, \lambda = 1.5$ and $q = 3, \lambda = 1.2$, the unperturbed pendulum system (3) bears the standard double well dynamics

with the coexistence of the homoclinic orbits of Duffing type and pendulum type. The natural difficulty, however, is that the analytical expressions of two types of homoclinic orbits cannot be obtained through simple formulas due to its irrational nonlinearity. We therefore introduce two types of approximate analytical solutions corresponding to Eqs. (10) and (12), and determine the parameters A_1, B_1, C_1 and A_2, B_2, C_2 by using numerical fitting to overcome the natural difficulty. To verify its approximation, Fig. 6 illustrates the comparisons between the numerical solution denoted by the black dotted line and the approximate analytical solution marked by red solid line. When $q = 3$ and $\lambda = 1.5$, the detailed comparisons of the solution $x_{\Gamma_1}^{hom1}(t)$ and $x_{\Gamma_1}^{hom2}(t)$ corresponding to the homoclinic orbits of Duffing type (*hom1*) and pendulum type (*hom2*) are plotted in Fig. 6a, b, where the approximate analytical solutions $x_{\Gamma_1}^{hom1}(t)$ and $x_{\Gamma_1}^{hom2}(t)$ can be derived by using numerical fitting and written as

$$\begin{aligned} x_{\Gamma_1}^{hom1}(t) &= -0.8081 \cot^{-1}(0.5609 \cosh(1.769 t)), \\ x_{\Gamma_1}^{hom2}(t) &= 2 \tan^{-1}(0.8234 \sinh(1.992 t)). \end{aligned} \tag{22}$$

Similarly, the comparisons between the numerical simulation denoted by black dotted line and the approximate analytical solution marked by red solid line are displayed for $q = 3$ and $\lambda = 1.2$ in Fig. 6c, d. The approximate analytical solutions $x_{\Gamma_1}^{hom1}(t)$ of the homoclinic orbits of Duffing type (*hom1*) and $x_{\Gamma_1}^{hom2}(t)$ of the homoclinic orbits of pendulum type (*hom2*) can be written as

$$\begin{aligned} x_{\Gamma_1}^{hom1}(t) &= -0.979 \cot^{-1}(0.235 \cosh(2.59 t)), \\ x_{\Gamma_1}^{hom2}(t) &= 2 \tan^{-1}(0.7538 \sinh(1.822 t)). \end{aligned} \tag{23}$$

As shown in Fig. 6, a good degree of correlation is demonstrated between the approximate analytical solution and the numerical solution of the homoclinic orbits of Duffing type and pendulum type; the details are shown in the corresponding captions. Based upon the Melnikov integrals corresponding to Eqs. (14), (15), (18) and (19), the Melnikovian detected chaotic boundary for the perturbed pendulum system (2) with

$q = 3, \lambda = 1.5$ is plotted by letting $f_0/\xi = R_{hom1}(\omega)$ and $f_0/\xi = R_{hom2}(\omega)$ in Fig. 7a. It is worth pointing out that the boundary curves of the homoclinic orbits of Duffing type (*hom1*) and pendulum type (*hom2*) obtained by Melnikov method are denoted by the solid line and the dashed line, respectively. Similarly, the chaotic boundary for the perturbed pendulum system (2) with $q = 3, \lambda = 1.2$ is plotted in Fig. 7b.

Then numerical simulations are utilized to detect the efficiency of the criteria obtained by Melnikov analysis, including bifurcation diagram, largest Lyapunov exponents, phase portraits, time history and Poincaré section. Figure 8a, c displays the bifurcation diagram for the external harmonic forcing f_0 versus angular displacement x with the theoretical threshold $f_0 = \overline{R_s}(\omega) \times \xi = 0.245$ and 0.158 marked by the solid line and the corresponding large Lyapunov exponents are plotted in Fig. 8b, d. Figure 8c shows that there exists a lot of chaos beyond the theoretical boundary 0.245 . Furthermore, two typical chaotic attractors can be presented for $f_0 = 0.3$ and $f_0 = 2.3$ in Fig. 8e, f, respectively. To be more precise, the corresponding stable (colored in red) and unstable (colored in blue) manifolds of a saddle point P near $(0, 0)$ and $(\pi, 0)$ are given in Fig. 8g, h, respectively, which indicates that the transversal intersections of the stable and unstable manifolds create the chaos in the sense of the Smale horseshoe.

To consider periodic solution and chaotic motion in more detail, the nonlinear dynamical technique is introduced. When $q = 3, \lambda = 1.5, \xi = 0.06$ and $\omega = 1.8$, Fig. 9a demonstrates a bifurcation diagram for the harmonic forcing f_0 versus angular displacement x with two detected criteria $f_0^{hom1} = \xi \times R_{hom1}(\omega) = 0.0456$ and $f_0^{hom2} = \xi \times R_{hom2}(\omega) = 0.3205$. Note that bifurcation diagrams colored in blue and red are calculated with different initial conditions $(x, y) = (1, 0)$ and $(-1, 0)$, respectively. Meanwhile, there exist various periodic windows and chaotic regions in Fig. 9a. It is obvious that non-chaotic range is observed below the chaotic boundary $f_0 = \xi \times \overline{R_s}(\omega) = 0.0456$ predicted by Melnikov analysis which is denoted by the solid line from this bifurcation diagram. In order to verify the chaotic zone, Fig. 9b shows the corresponding largest Lyapunov exponents with the initial condition $(-1, 0)$. It is found that a good degree of correlation is demonstrated between the bifurcation diagram (Fig. 9a) and Lyapunov exponents (Fig. 9b). When parameter f_0 enlarges beyond above threshold value

0.0456 reaching around 0.34, the system jumps to a chaotic motion from a pair of coexisting period-1 solutions and a pair of coexisting period-2 solutions. Notice that these two coexisting period-1 solutions, colored in red and blue, are symmetrical and the phase portraits orbits for $f_0 = 0.1$ are presented in Fig. 10a, the corresponding Poincaré section are marked by the yellow solid point and the green solid point, respectively. Clearly, the time history of a pair of period-1 solutions are displayed with red and blue solid lines in Fig. 10b. A period-3 solution [34] occurs at $f_0 = 0.6$, while the corresponding phase portrait marked by black curve and Poincaré section denoted by green points is displayed in Fig. 10c, and the corresponding time history of the period-3 solution is plotted in Fig. 10d. Meanwhile, the digits are introduced to describe the law of periodic motions. As parameter f_0 increases, the different types of chaotic motions of this system (2) are calculated for $f_0 = 0.65$ and 1.6, the corresponding chaotic attractors are displayed in Fig. 10e, g, respectively. Owing to the coupling of simple pendulum and SD oscillator, the chaotic attractor depicted in Fig. 10e bears significant similarities to the structure of SD attractor, which means that the pendulum ball will swing irregularly; the details are shown in [43]. Clearly, the chaotic attractor shown in Fig. 10g is similar to the coupling of pendulum attractor and SD attractor, which represents the mixed motions of irregular oscillation and rotation. Furthermore, the corresponding time histories are shown in Fig. 10f, h, and the law of chaotic motions are labeled including oscillation and rotation, respectively.

Similarly, the bifurcation diagram is given for f_0 versus x with two detected criteria $f_0^{hom1} = \xi \times R_{hom1}(\omega) = 0.0434$ and $f_0^{hom2} = \xi \times R_{hom2}(\omega) = 0.1918$ for parameters $q = 3$, $\lambda = 1.2$, $\xi = 0.04$, $\omega = 1.5$ in Fig. 9c. The bifurcation diagrams colored in blue and red start from different initial conditions $(x, y) = (1, 0)$ and $(-1, 0)$, respectively, from which the existence of a pair of period doubling series and chaotic windows can be seen. From this bifurcation diagram, no chaotic motion is observed below the chaotic boundary $f_0 = \xi \times \bar{R}_s(\omega) = 0.0434$ predicted by Melnikov method which is marked by the solid line. The corresponding largest Lyapunov exponents is plotted from the initial condition $(-1, 0)$ in Fig. 9d. These two coexisting period-4 solutions and two coexisting period-3 solutions [34], colored red and blue, are symmetrical, the orbits for $f_0 = 0.58$ and 0.9 are presented in Fig. 11a, c, and the corresponding Poincaré section

are marked by the yellow solid points and the green solid points, respectively. Time histories are shown in Fig. 11b, d, of which the law of motion is described with the digits. When $f_0 = 0.65$, this system (2) exhibits chaotic motion, of which the chaotic attractor is given in Fig. 11e and the corresponding time history is plotted in Fig. 11f. From the time history diagram, the system exhibits the irregular oscillating and rotational motions; however, the oscillating movement dominates and the rotation movement occasionally appears; the details are shown in Fig. 11f. Unlike the above chaotic motion, the dominance of the irregular rotation in the whole chaotic movement is presented, whose chaotic attractor is calculated in Fig. 11g and the corresponding time history is displayed in Fig. 11h.

To further detect the rationality of the chaotic boundary derived by Melnikov method, for $q = 3$, $\lambda = 1.2$, $\xi = 0.04$, Fig. 12 shows a two-dimensional parameter space plot in the range of $\omega \in [0, 4]$ and $f_0 \in [0, 2]$. The red and white regions depicted in Fig. 12, which can be plotted by calculating the largest Lyapunov exponents, correspond to the chaotic region with positive Lyapunov exponent and non-chaotic region. For example, the parameters f_0 and ω take the value of red region which means that the system exhibits a chaotic motion and its largest Lyapunov exponents is a positive value. With the help of the Melnikov integrals Eqs. (14), (15), (18) and (19), the Melnikovian to predict the border of chaos for the perturbed pendulum system (2) are plotted by letting $f_0 = R_{hom1}(\omega) \times \xi$ (black solid curve) and $f_0 = R_{hom2}(\omega) \times \xi$ (black dashed curve), as shown in Fig. 12. Moreover, the theoretical threshold of chaotic region marked by the green curve can be plotted by calculating $f_0 = \bar{R}_s(\omega) \times \xi$. It is found that the chaotic region corresponding to the red region shows a good agreement with the theoretical analysis satisfying $f_0 > \bar{R}_s(\omega) \times \xi$. It is worth reiterating here that the numerical studies have been presented by using MATLAB and DYNAMICS [50] softwares which allows one to investigate the nonlinear dynamic behaviors by considering the time history, bifurcation diagram, Poincaré map, Lyapunov exponents and parameter space plot.

4.2 Melnikov analysis for the discontinuous system

When the geometrical parameter λ decreases to 1 from the mathematical point of view, the rotating pendulum

Fig. 10 (Color online) When $q = 3$, $\lambda = 1.5$, $\xi = 0.06$, $\omega = 1.8$, **a** phase portraits and their Poincaré section of a pair of period-1 solutions for $f_0 = 0.1$, **b** corresponding time histories $x(t)$, **c** phase portrait and its Poincaré section of a period-3 solution for $f_0 = 0.6$, **d** corresponding time history $x(t)$, **e** chaotic attractor of SD type for $f_0 = 0.95$ and the corresponding time history **(f)**, **g** chaotic attractor of pendulum type for $f_0 = 1.78$ and its time history **(h)**, respectively

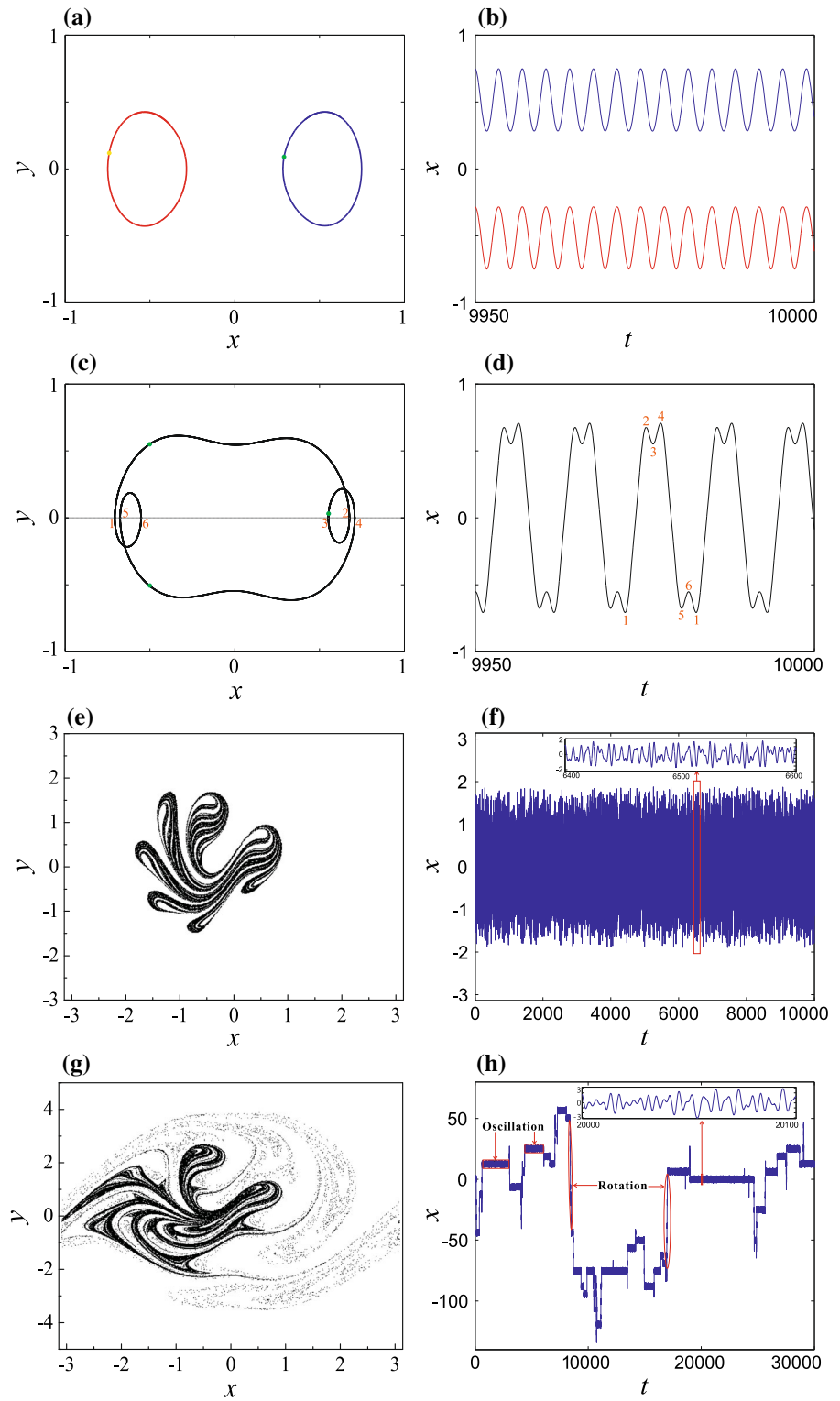
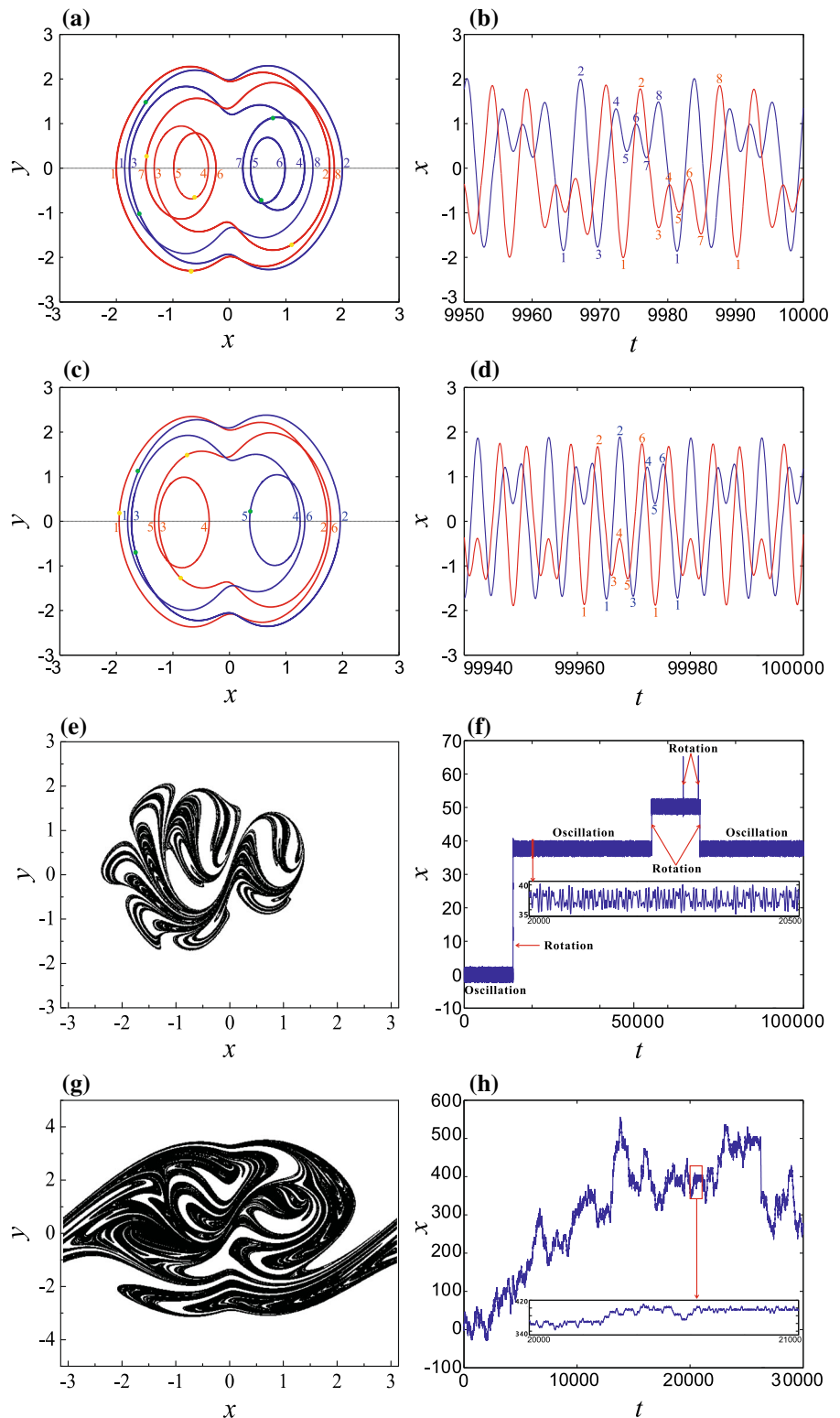


Fig. 11 (Color online) When $q = 3$, $\lambda = 1.2$, $\xi = 0.04$, $\omega = 1.5$, **a** the phase portraits and their Poincaré section of a pair of period-4 solutions for $f_0 = 0.58$, **b** the corresponding time histories $x(t)$, **c** the phase portraits of a pair of period-3 solutions and their Poincaré section for $f_0 = 0.9$, **d** the corresponding time histories $x(t)$, **e** the chaotic attractor for $f_0 = 1.6$ and its time history (**f**), **g** the chaotic attractor for $f_0 = 1.6$ and its time history (**h**), respectively



system (1) becomes a non-smooth dynamical system with a discontinuous nonlinear restoring force. The chaotic dynamics [42, 51] for the limit case of this pendulum system is studied by using the numerical technique in this subsection. This non-smooth dynamical system can be described as a piecewise smooth system and written as

$$\begin{cases} \dot{x} = y \\ \dot{y} = f_0 \cos \omega t - \xi \dot{x} + \begin{cases} -(1+q) \sin x + q \cos \frac{x}{2}, & x \in (0, \pi] \\ 0, & x = 0 \\ -(1+q) \sin x - q \cos \frac{x}{2}, & x \in (-\pi, 0). \end{cases} \end{cases} \tag{24}$$

It is worth pointing out that the phase space is divided into two parts denoted by Σ_+ and Σ_- by the line $x = 0$. Furthermore, the details of solutions $x_{\Gamma_{1,2}}^{Dhom1}(t)$ for the homoclinic orbits of SD type connecting a nonstandard saddle point $(0, 0)$ with blue are shown in Figs. 13 or 5b, of which the main mathematical features for $\exists T_0 > 0$ satisfy

$$\left\{ \left(x_{\Gamma_{1,2}}^{Dhom1}(t), y_{\Gamma_{1,2}}^{Dhom1}(t) \right) \mid (x(t), y(t)) \in \Sigma_{\pm}, t \in (-T_0, T_0) \right\} \cup (0, 0). \tag{27}$$

We only consider one period $x \in (-\pi, \pi]$ for system (24) due to the periodic nature. Note that the dynamic behaviors of the unperturbed discontinuous system is similar to simple pendulum coupled with SD oscillator with the coexistence of the nonstandard homoclinic orbits of SD type and pendulum type in Sect. 3. The phase trajectories of the nonstandard homoclinic orbits of SD type (blue) and pendulum type (red) are plotted in Fig. 13 and the corresponding implicit function expressions are

Moreover, the details of solutions $x_{\Gamma_{1,2}}^{hom2}(t)$ for the homoclinic orbits of pendulum type connecting two saddle point $(\pm\pi, 0)$ with red are shown in Figs. 13 or 5b, of which the main mathematical features satisfy

$$\Gamma_{1,2}^{Dhom1}(x, y) = \begin{cases} \Sigma_+ : \left\{ (x, y) \mid \frac{y^2}{2} - (1+q) \cos x - 2q \sin \frac{x}{2} + q + 1 = 0 \right\}, \\ x = 0 : (x, y) = (0, 0), \\ \Sigma_- : \left\{ (x, y) \mid \frac{y^2}{2} - (1+q) \cos x + 2q \sin \frac{x}{2} + q + 1 = 0 \right\}, \end{cases} \tag{25}$$

and

$$\Gamma_{1,2}^{Dhom2}(x, y) = \begin{cases} \Sigma_+ : \left\{ (x, y) \mid \frac{y^2}{2} - (1+q) \cos x - 2q \sin \frac{x}{2} + q - 1 = 0 \right\}, \\ x = 0 : (x, y) = (0, \pm\beta), \\ \Sigma_- : \left\{ (x, y) \mid \frac{y^2}{2} - (1+q) \cos x + 2q \sin \frac{x}{2} + q - 1 = 0 \right\}. \end{cases} \tag{26}$$

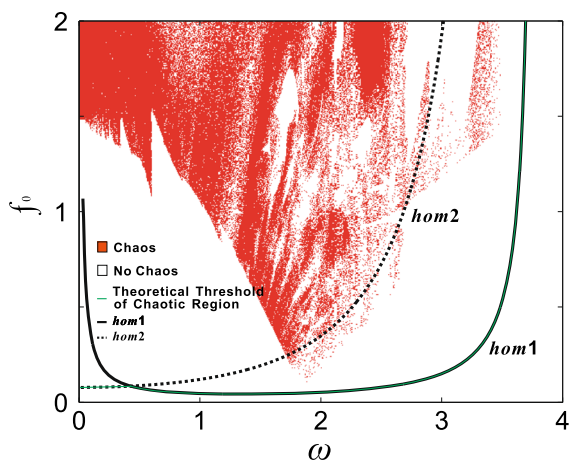


Fig. 12 A two-dimensional parameter space plot for $q = 3$, $\lambda = 1.2$, $\xi = 0.04$ in the range of $f_0 \in [0, 2]$ and $\omega \in [0, 4]$ and two chaotic boundaries (*hom1* and *hom2*) derived by Melnikov analysis (the red region corresponds to the chaotic region, the white region represents non-chaotic region and the green curve $f_0 = 0.04 \times \bar{R}_s(\omega)$ is the theoretical boundary of chaos)

$$\left\{ \left(x_{\Gamma_{1,2}}^{Dhom2}(t), y_{\Gamma_{1,2}}^{Dhom2}(t) \right) \mid (x(t), y(t)) \in \Sigma_{\pm}, t \in (-\infty, 0) \cup (0, +\infty) \right\} \cup (0, \pm\beta). \tag{28}$$

We define that the trajectory crossing two planes Σ_+ and Σ_- is continuous at point $x = 0$, so the non-smooth homoclinic orbits should satisfy

$$\begin{aligned} \lim_{t \rightarrow \pm T_0} x_{\Gamma_{1,2}}^{Dhom1}(t) &= 0, \quad \lim_{t \rightarrow \pm T_0} y_{\Gamma_{1,2}}^{Dhom1}(t) \\ &= 0, \quad \lim_{t \rightarrow 0} x_{\Gamma_{1,2}}^{Dhom1}(t) = \mp\alpha, \end{aligned} \tag{29}$$

$$\begin{aligned} \lim_{t \rightarrow 0} x_{\Gamma_{1,2}}^{Dhom2}(t) &= 0, \quad \lim_{t \rightarrow 0} y_{\Gamma_{1,2}}^{Dhom2}(t) \\ &= \pm\beta, \quad \lim_{t \rightarrow +\infty} x_{\Gamma_{1,2}}^{Dhom2}(t) = \mp\pi. \end{aligned} \tag{30}$$

Due to the non-smooth characteristics at $t = T_0$ of the solutions $x_{\Gamma_{1,2}}^{Dhom1}(t)$ for the homoclinic orbits of SD type, the numerical technique is utilized to calculate chaotic thresholds in the perturbed discontinuous system.

Clearly, $y_{\Gamma_{1,2}}^{Dhom1}(t)$ is odd function, so the Melnikov function (8) for the homoclinic orbits of SD type marked by blue in Fig. 5b can be expressed as

$$M_{Dhom1}(\tau) = \lim_{\epsilon \rightarrow 0} \left\{ -\xi \int_{-(T_0-\epsilon)}^{T_0-\epsilon} (y_{\Gamma_{1,2}}^{Dhom1}(t))^2 dt - f_0 \sin \omega\tau \int_{-(T_0-\epsilon)}^{T_0-\epsilon} y_{\Gamma_{1,2}}^{Dhom1}(t) \sin \omega t dt \right\}. \tag{31}$$

where $x_{\Gamma_{1,2}}^{Dhom1}(\pm(T_0 - \epsilon)) = \mp\epsilon$, as shown in Fig. 13. Note that $y_{\Gamma_{1,2}}^{Dhom2}(t)$ is a continuous even function for $t \in (-\infty, +\infty)$, the corresponding Melnikov function (8) of the homoclinic orbits of pendulum type marked by red in Fig. 5b become

$$\begin{aligned} M_{Dhom2}(\tau) &= -\xi \int_{-\infty}^{+\infty} (y_{\Gamma_{1,2}}^{Dhom2}(t))^2 dt \\ &\quad + f_0 \cos \omega\tau \int_{-\infty}^{+\infty} y_{\Gamma_{1,2}}^{Dhom2}(t) \cos \omega t dt. \end{aligned} \tag{32}$$

With the aid of Hamiltonian function (7), we have

$$\begin{aligned} \frac{dx_{\Gamma_{1,2}}^{Dhom1}(t)}{dt} \\ = \mp\sqrt{2(1+q)\cos x + 2q\sqrt{2-2\cos x} - 2q - 2}, \end{aligned} \tag{33}$$

$$\begin{aligned} \frac{dx_{\Gamma_{1,2}}^{Dhom2}(t)}{dt} \\ = \pm\sqrt{2(1+q)\cos x + 2q\sqrt{2-2\cos x} - 2q + 2}. \end{aligned} \tag{34}$$

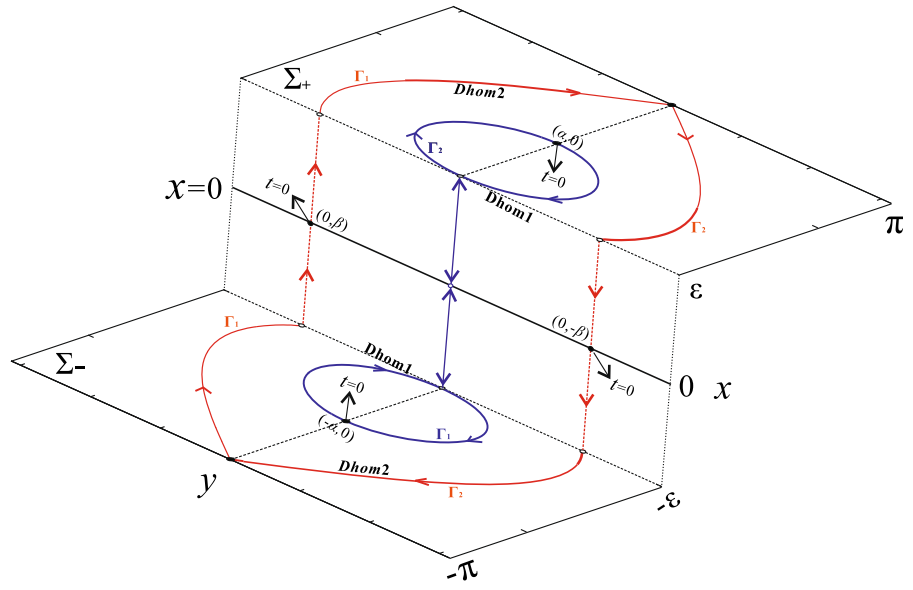
Based upon Eqs. (33) and (34), the integrating equation yields

$$t = \int_{\pm\alpha}^x \frac{d\varphi}{\mp\sqrt{2(1+q)\cos \varphi + 2q\sqrt{2-2\cos \varphi} - 2q - 2}} > 0, \tag{35}$$

$$t = \int_0^x \frac{d\varphi}{\pm\sqrt{2(1+q)\cos \varphi + 2q\sqrt{2-2\cos \varphi} - 2q + 2}} > 0. \tag{36}$$

Let us substitute Eqs. (33) and (35) into Eq. (31), the Melnikov integrals for the homoclinic orbits of SD type can be obtained and expressed as

Fig. 13 (Color online) Phase trajectories of the nonstandard homoclinic orbits of SD type ($Dhom1$) and pendulum type ($Dhom2$) for the discontinuous system. Note that the trajectory is smooth for $(x, y) \in \Sigma_+ \cup \Sigma_-$, while the trajectory is non-smooth for $x = 0$



$$\begin{aligned}
 I_1^{Dhom1} &= \lim_{\epsilon \rightarrow 0} \int_{-(T_0-\epsilon)}^{T_0-\epsilon} (y_{\Gamma_{1,2}}^{Dhom1}(t))^2 dt = 2 \lim_{\epsilon \rightarrow 0} \int_{\pm\alpha}^{\pm\epsilon} y_{\Gamma_{1,2}}^{Dhom1}(x) dx \\
 &= 2 \lim_{\epsilon \rightarrow 0} \int_{\epsilon}^{\alpha} \sqrt{2(1+q) \cos x + 2q\sqrt{2-2\cos x} - 2q - 2} dx, \tag{37}
 \end{aligned}$$

$$\begin{aligned}
 I_2^{Dhom1} &= \lim_{\epsilon \rightarrow 0} \int_{-(T_0-\epsilon)}^{T_0-\epsilon} y_{\Gamma_{1,2}}^{Dhom1}(t) \sin \omega t dt = 2 \lim_{\epsilon \rightarrow 0} \int_{\pm\alpha}^{\pm\epsilon} \sin \omega t dx \\
 &= 2 \lim_{\epsilon \rightarrow 0} \int_{\epsilon}^{\alpha} \sin \left(\omega \int_{\alpha}^x \frac{d\varphi}{\sqrt{2(1+q) \cos \varphi + 2q\sqrt{2-2\cos \varphi} - 2q - 2}} \right) dx. \tag{38}
 \end{aligned}$$

Letting $M_{Dhom1}(\tau) = 0$, there exists simple zero for τ if and only if the following inequality holds:

$$\frac{f_0}{\xi} > \left| \frac{I_1^{Dhom1}}{I_2^{Dhom1}} \right| = R_{Dhom1}(\omega). \tag{39}$$

Similarly, the Melnikov integrals for the homoclinic orbits of pendulum type can be derived by substituting Eqs. (34) and (36) into Eq. (32), and written as

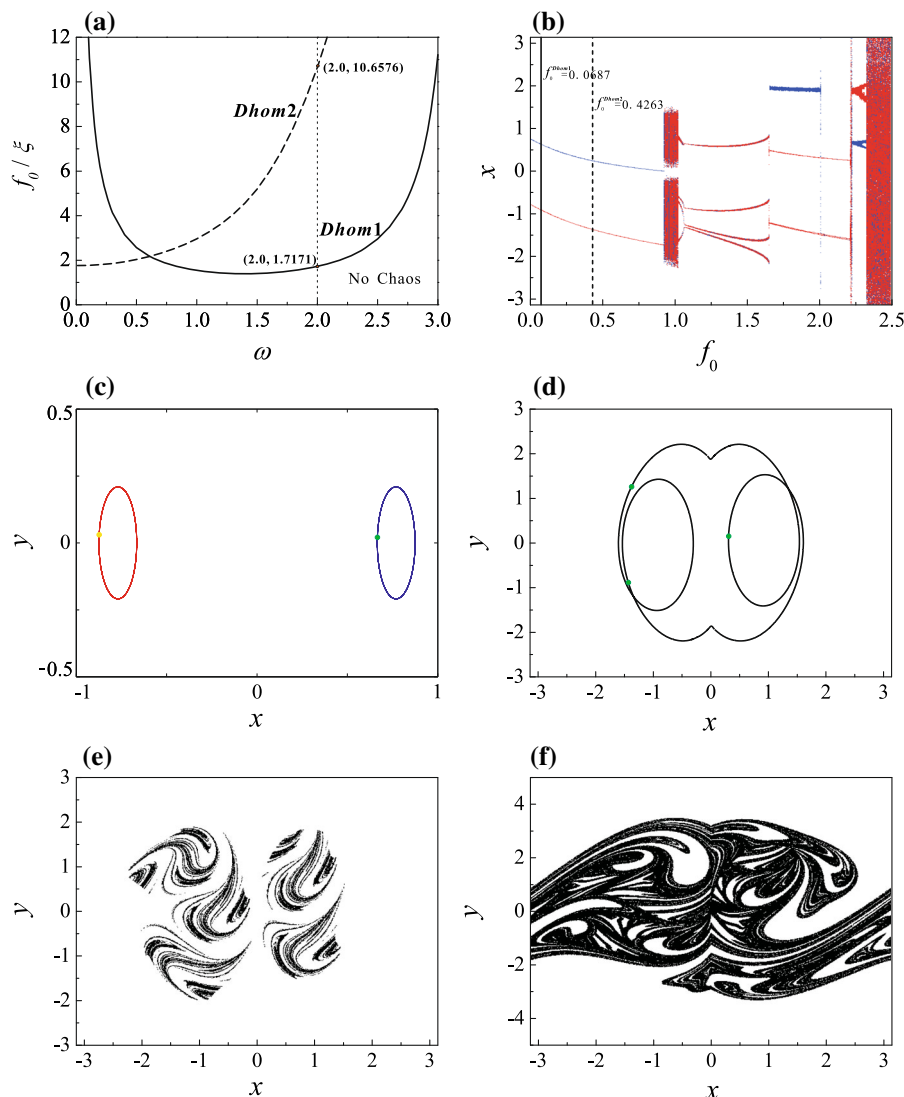
It is concluded that $M_{Dhom2}(\tau) = 0$ possesses simple zero for τ if and only if the following inequality holds:

$$\frac{f_0}{\xi} > \left| \frac{I_1^{Dhom2}}{I_2^{Dhom2}} \right| = R_{Dhom2}(\omega); \tag{42}$$

$$\begin{aligned}
 I_1^{Dhom2} &= \int_{-\infty}^{+\infty} (y_{\Gamma_{1,2}}^{Dhom2}(t))^2 dt = \int_{\mp\pi}^{\pm\pi} y_{\Gamma_{1,2}}^{Dhom2}(x) dx; \\
 &= 2 \int_0^{\pi} \sqrt{2(1+q) \cos x + 2q\sqrt{2-2\cos x} - 2q + 2} dx, \tag{40}
 \end{aligned}$$

$$\begin{aligned}
 I_2^{Dhom2} &= \int_{-\infty}^{+\infty} y_{\Gamma_{1,2}}^{Dhom2}(t) \cos \omega t dt = \int_{\mp\pi}^{\pm\pi} \cos \omega t dx \\
 &= 2 \int_0^{\pi} \cos \left(\omega \int_0^x \frac{d\varphi}{\sqrt{2(1+q) \cos \varphi + 2q\sqrt{2-2\cos \varphi} - 2q + 2}} \right) dx. \tag{41}
 \end{aligned}$$

Fig. 14 (Color online) When $q = 3, \lambda = 1, \xi = 0.04, \omega = 2$, **a** the chaotic thresholds of the homoclinic orbits of SD type denoted by the solid line ($f_0/\xi = R_{hom1}(\omega)$) and the homoclinic orbits of pendulum type denoted by the dashed line ($f_0/\xi = R_{hom2}(\omega)$), **b** the bifurcation diagram for f_0 versus x with the thresholds $f_0^{Dhom1} = 0.0687$ marked by solid line and $f_0^{Dhom2} = 0.4263$ marked by dash line, **c** the phase portraits and their Poincaré section of a pair of period-1 solutions for $f_0 = 0.06$, **d** the phase portrait and its Poincaré section of a period-3 solution for $f_0 = 2$, **e** and **f** the chaotic attractors of discontinuous case for $f_0 = 0.95$ and $f_0 = 2.5$, respectively



where the parameters α and β in Eqs. (35) and (38) denoted in Fig. 5b satisfy the following equations

$$\alpha = \arccos \left| \frac{1 + 2q - q^2}{(1 + q)^2} \right|, \quad \beta = 2. \tag{43}$$

So as to detect the chaotic boundary of perturbed discontinuous system, we define the function

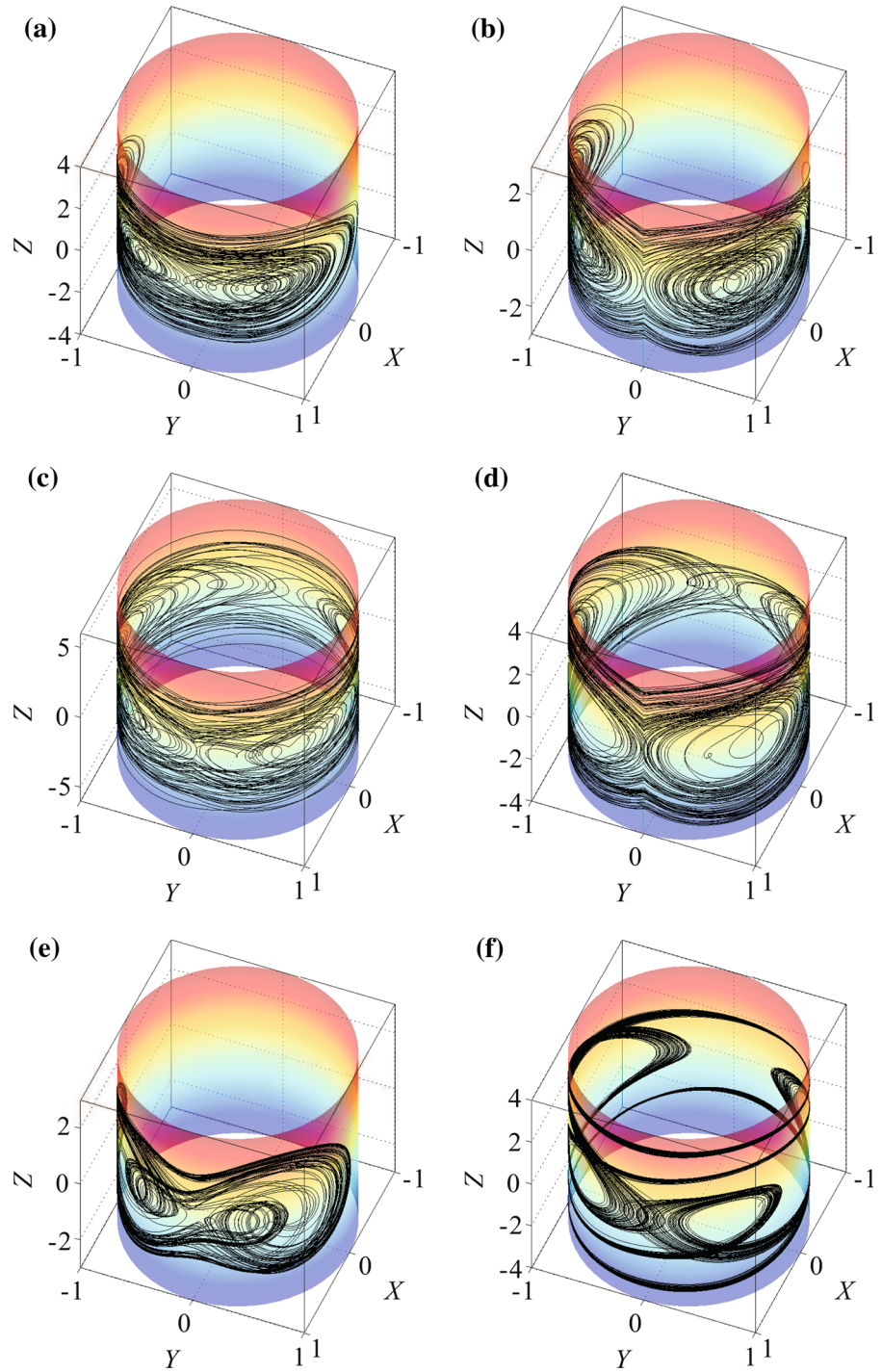
$$\bar{R}_D(\omega) = \min\{R_{Dhom1}(\omega), R_{Dhom2}(\omega)\}. \tag{44}$$

It is clear that the non-chaotic region can be given for the parameters satisfying $f_0/\xi < \bar{R}_D(\omega)$, while

the chaotic motion must exist in the region satisfying $f_0/\xi > \bar{R}_D(\omega)$.

Then the numerical simulations are utilized to detect the efficiency of the criteria. The boundaries detected by the Melnikov for the perturbed discontinuous system are plotted by letting $f_0/\xi = R_{Dhom1}(\omega)$ and $f_0/\xi = R_{Dhom2}(\omega)$, which are marked by solid and dashed lines in Fig. 14a, respectively. For parameters $q = 3, \lambda = 1, \xi = 0.04, \omega = 2$ taken fixed, Fig. 14b presents a bifurcation diagram for f_0 versus x starting with different initial conditions (1,0) colored in blue and (-1,0) colored in red, respectively. As can be seen in this bifurcation diagram, the non-chaotic region is observed below the boundary $f_0 =$

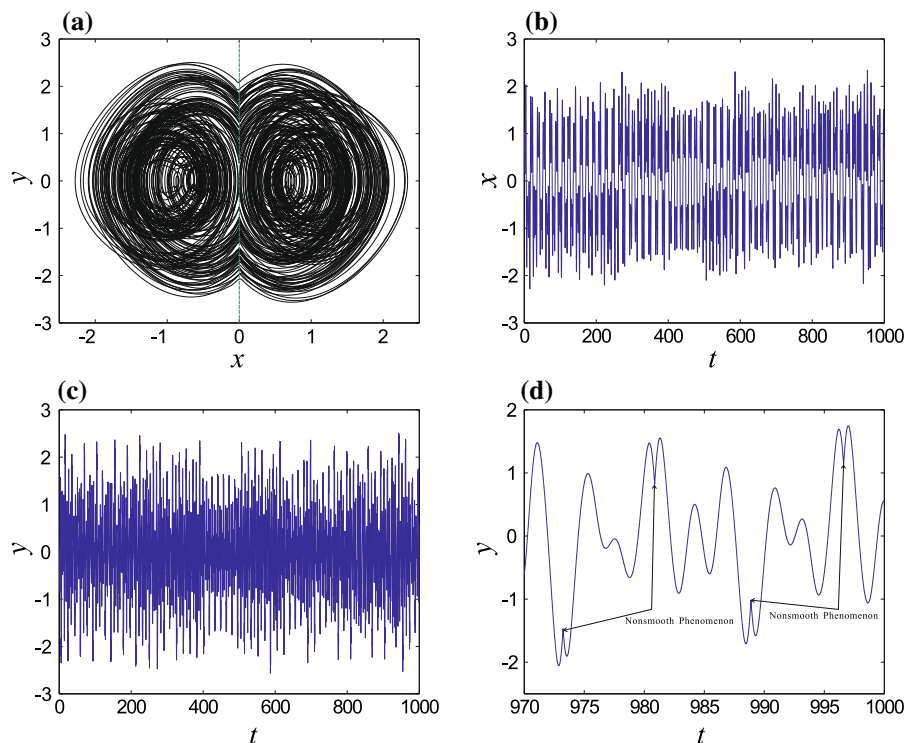
Fig. 15 (Color online) Cylindrical phase portraits of the chaotic motions in the perturbed pendulum system. **a** Oscillation of smooth case for $q = 3, \lambda = 1.5, \xi = 0.06, \omega = 1.8, f_0 = 0.95$, **b** the oscillation of discontinuous case for $q = 3, \lambda = 1, \xi = 0.04, \omega = 2, f_0 = 0.95$, **c** the oscillation and rotation of smooth case for $q = 3, \lambda = 1.5, \xi = 0.06, \omega = 1.8, f_0 = 1.78$, **d** the oscillation and rotation of discontinuous case for $q = 5, \lambda = 1, \xi = 0.4, \omega = 1.5, f_0 = 2$, **e** $q = 8, \lambda = 1.5, \xi = 0.5, \omega = 1, f_0 = 2$, **f** $q = 2, \lambda = 1.5, \xi = 0.5, \omega = 1, f_0 = 2$



$\xi \times \bar{R}_D(\omega) = 0.0687$ calculated by Melnikov method which is denoted by the solid line. While the parameter f_0 enlarges beyond above boundary value 0.0687 reaching around 0.85, the pendulum jumps to a chaotic

motion starting from a pair of period-1 motions, of which phase portraits and their Poincaré sections can be depicted in Fig. 14c. Moreover, the phase portrait marked by black solid line and its Poincaré section

Fig. 16 (Color online) Non-smooth chaotic motion, **a** phase portrait for $t \in [0, 1000]$ starting from initial condition $(1, 0)$, **b** and **c** time histories $x(t)$ and $y(t)$, **d** time history $y(t)$ with non-smooth points



denoted by green solid points of the periodic-3 solution are displayed; the details are shown in Fig. 14d. The oscillating chaotic attractor of perturbed discontinuous system can be calculated in Fig. 14e for parameter $f_0 = 0.65$. When parameter $f_0 = 2.5$, the discontinuous chaotic attractor of the oscillation coupled with rotation is calculated as shown in Fig. 14f.

4.3 Cylindrical phase portraits for different types of chaotic motions

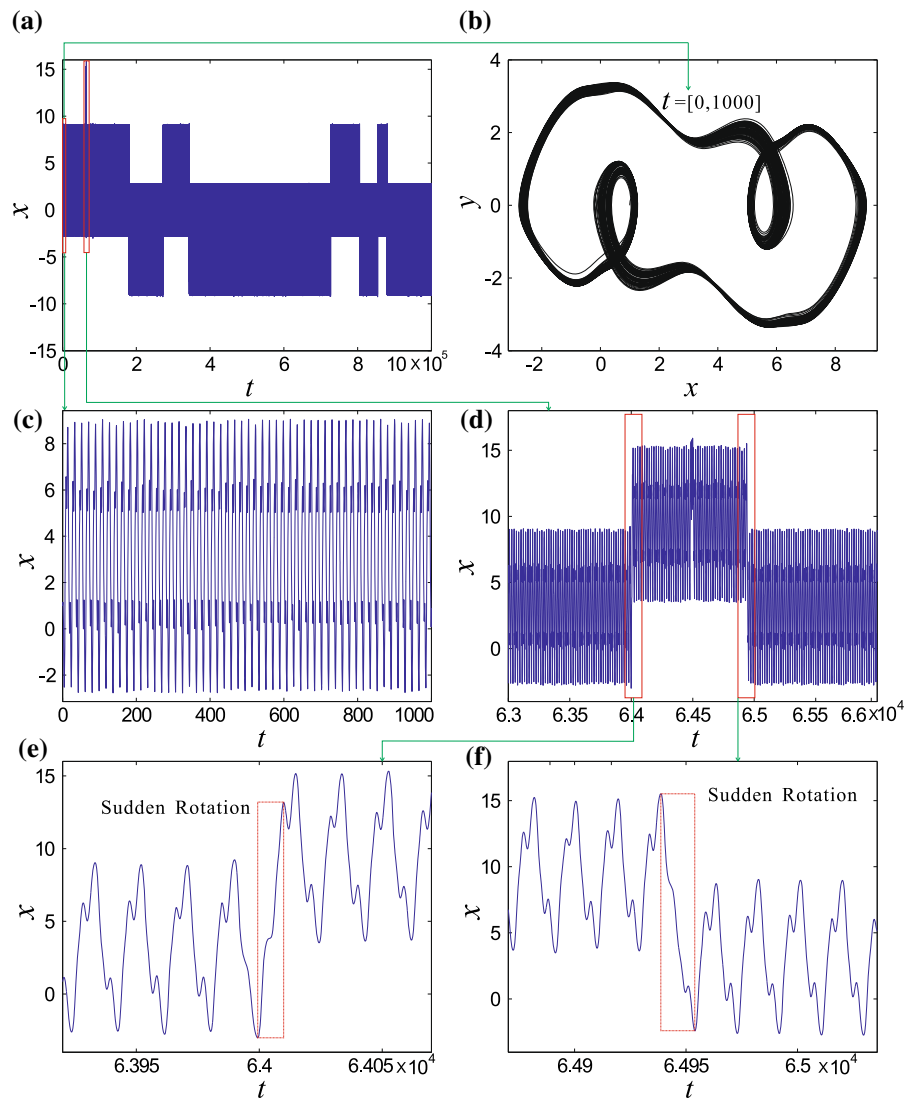
The perturbed rotating pendulum system (2) exhibits different types of chaotic motions due to the tight coupling nonlinearities of simple pendulum (Rotation) and SD oscillator (Oscillation). In order to describe different kinds of chaotic motions, the analysis of cylindrical phase portraits is introduced to effectively distinguish the rotational motion (trajectory twining around the cylinder) with the oscillating motion (trajectory attaching to the surface of the cylinder) by means of the mapping $X = \cos x$, $Y = \sin x$, $Z = \dot{x}$ in this subsection.

Figure. 15a presents a phase portrait on the unit cylinder marked by black solid line, which seems to attach the phase portrait to the surface of unit cylinder.

Such cylindrical phase portrait in the perturbed smooth system (2) represents the chaotic motion characterized by oscillation. The cylindrical phase portrait in Fig. 15a implies that pendulum ball does an irregular reciprocating movement near the equilibrium x_1 . Particularly, the chaotic motion characterized by oscillation in the perturbed discontinuous system is illustrated in Fig. 15b, whose the phase trajectories show non-smooth dynamics at the line colored in blue. Obviously, the cylindrical phase portrait of the chaotic motion characterized by the coexistence of rotation and oscillation in the perturbed smooth system is displayed in Fig. 15c, which means that pendulum ball does both the irregular reciprocating movement and the irregular rotating movement around the point A depicted in Fig. 1. For the perturbed discontinuous system, Fig. 15d shows the cylindrical phase portrait for the chaotic motion characterized by the coexistence of rotation and oscillation. In addition, different kinds of chaotic motions of the perturbed smooth system (2) are described in Fig. 15e, f. The details of the parameters taken in Fig. 15 can be found in the corresponding captions.

The cylindrical phase diagram is an effective way to distinguish between rotation and oscillation in the perturbed rotating pendulum system (2). Note that the

Fig. 17 (Color online) Chaotic motion for $q = 2, \lambda = 1.5, \xi = 0.5, \omega = 1, f_0 = 2$, **a** the time history $x(t)$ for $t \in [0, 1000000]$, **b** the phase portrait in the xy plane for $t \in [0, 1000]$ and the corresponding time history (c), **d** the time history $x(t)$ for $t \in [63000, 66000]$, **e** and **f** two enlarged images of time history with sudden rotation



cylindrical phase portraits depicted in Fig. 15b, f show novel nonlinear phenomena which allows us to explore more deeply in the complex chaotic motion of pendulum system. Figure 15b describes the cylindrical phase portrait of non-smooth oscillating chaotic motion and the corresponding phase portrait in the xy plane is plotted in Fig. 16a. For a better understanding of non-smooth feature, two time histories $x(t)$ and $y(t)$ are displayed for $t \in [0, 1000]$, as shown in Fig. 16b, c. Clearly, there exist many non-smooth points in time history $y(t)$; the details are shown in Fig. 16d. Interestingly, Fig. 15f presents novel cylindrical phase portrait for $t \in [0, 1000]$ which looks like a quasi-periodic solution. It is found that, however, the motion of pendu-

lum system is chaos when we take enough time for $x(t)$. For $t \in [0, 1000000]$, the time history $x(t)$ is calculated in Fig. 17a. When $t \in [0, 1000]$, the phase portrait in the xy plane and the corresponding time history are plotted in Fig. 17b, c, respectively. Because the time t is too short to observe the nature of its motion, according to Fig. 17b, c, we may mistake it for a quasi-periodic solution. To explore this chaotic motion, we consider the time history in this interval $t \in [63000, 66000]$ where time history has changed dramatically for the first time, shown in Fig. 17d. Notice that the pendulum takes place a sudden rotational motion at some uncertain time which breaks the so-called quasi-periodic motion; the details are shown in Fig. 17e, f.

5 Conclusion

The chaotic dynamics of the rotating pendulum system with bistable characteristics under the perturbations of the viscous damping and harmonic forcing is studied in this paper. An effective technique for testing the chaotic thresholds arising from the coexistence of the homoclinic orbits of Duffing-type and pendulum-type tangling is presented in the perturbed smooth system, which allows us to semi-analytically derived the chaotic thresholds of the complicated nonlinear system. More precisely, two types of the approximate analytical solutions corresponding to the homoclinic orbits of Duffing type and pendulum type are introduced to avoid the barrier of the associated irrational nonlinearity, of which Melnikov integrals can be analytically calculated. Notice that the homoclinic orbits of SD type has a substantial departure in the dynamics from the standard one, for which a numerical technique is carried out to detect the chaotic thresholds of the perturbed discontinuous system. The efficiency of the proposed techniques has been presented by using numerical simulations including the bifurcation diagram, Lyapunov exponents, phase portraits, time history and Poincaré section, which clearly demonstrates the predicated chaotic attractors. The results obtained herein provide an effective technique for testing the chaotic thresholds in nonlinear dynamical system without solving the analytical expression of the singular closed trajectory and calculating the complicated Melnikov integrals. With the help of cylindrical phase portraits, different types of chaos can be classified including oscillation, rotation and coexistence of oscillation and rotation. An undetectable chaos which bears significant similarity of quasi-periodic motion is studied with sudden rotation. The future study on the rotating pendulum system with bistable characteristics is being carried out by the current authors in two application aspects: The first is the resonance analysis [52,53] and the second are the vibration isolation [54,55] and the energy absorption [56].

Acknowledgements This work was supported by the National Natural Science Foundation of China (Grant Nos. 11702078, 11771115); the Natural Science Foundation of Hebei Province (Grant Nos. A2018201227, A2019402043); and the High-Level Talent Introduction Project of Hebei University (801260201111).

Compliance with ethical standards

Conflict of interest The authors declare that they have no conflict of interest.

Appendix

When $f_0 = 0$ and $\omega = 0$, the damping pendulum system can be written as

$$\begin{cases} \dot{x} = y, \\ \dot{y} = -\xi y - \sin x - q\lambda \sin x \left(1 - \frac{1}{\sqrt{1 + \lambda^2 - 2\lambda \cos x}} \right). \end{cases}$$

This study focuses on the rotating pendulum system with bistable characteristics which means that there exist five equilibria $(x_i, y_i)_{i=1,2,3,4,5}$ in the damping pendulum system satisfying $|\rho| < 1$ or

$$\left\{ (\lambda, q) \mid q > \frac{\lambda - 1}{\lambda(2 - \lambda)}, \lambda \in (1, 2), q \in (0, +\infty) \right\}.$$

Then, the Jacobian matrix at equilibria $(x_i, y_i)_{i=1,2,3,4,5}$ can be expressed as

$$J_{(x_i, y_i)} = \begin{bmatrix} 0 & 1 \\ K(x) & -\xi \end{bmatrix},$$

and

$$K(x) = -(1 + q\lambda) \cos x + \frac{q\lambda \cos x}{\sqrt{1 + \lambda^2 - 2\lambda \cos x}} - q\lambda^2 \sin^2 x \left(1 + \lambda^2 - 2\lambda \cos x \right)^{-1.5},$$

which leads to the characteristic equation

$$\Lambda^2 + \xi \Lambda - K(x_i) = 0.$$

Two eigenvalues $\Lambda_{1,2}$ can be derived by calculating the characteristic equation and written as

$$\Lambda_{1,2} = \frac{-\xi \pm \sqrt{\xi^2 + 4K(x_i)}}{2},$$

where

$$\begin{aligned} \Delta &= \xi^2 + 4K(x_i), \quad K(x_1) \\ &= q \frac{\lambda(2 - \lambda)}{\lambda - 1} - 1 > 0, \\ K(x_{2,3}) &= 1 + \frac{q\lambda^2}{1 + \lambda} > 0, \quad K(x_{4,5}) \\ &= -\frac{(1 - \rho^2)(1 + q\lambda)^3}{q^2\lambda} < 0. \end{aligned}$$

Then, we will explore the effect of nonnegative damping ξ on the equilibria $(x_i, y_i)_{i=1,2,3,4,5}$ based upon two eigenvalues. The detailed analysis is listed in the following.

(a) When $\xi > 0$ and $\xi = 0$, for the equilibria (x_1, y_1) , (x_2, y_2) and (x_3, y_3) , there exist two unequal real roots

$$\Lambda_{1,2} = \frac{-\xi \pm \sqrt{\xi^2 + 4K(x_{1,2,3})}}{2}, \quad \Lambda_{1,2} = \pm \sqrt{K(x_{1,2,3})}.$$

due to $\Delta > 0$ and $K(x_{1,2,3}) > 0$. It is concluded that the equilibria (x_1, y_1) , (x_2, y_2) and (x_3, y_3) are saddle points.

(b) No damping: When $\xi = 0$, for the equilibria (x_4, y_4) and (x_5, y_5) , there exists a pair of conjugate pure virtual roots

$$\Lambda_{1,2} = \pm \sqrt{-K(x_{4,5})} i.$$

due to $\Delta < 0$ and $K(x_{4,5}) < 0$. It is concluded that (x_4, y_4) and (x_5, y_5) are centers.

(c) Weak damping: When $\xi^2 + 4K(x_{4,5}) < 0$, for the equilibria (x_4, y_4) and (x_5, y_5) , there exists a pair of conjugate virtual roots

$$\Lambda_{1,2} = \frac{-\xi \pm \sqrt{-\xi^2 - 4K(x_{1,2,3})}}{2} i$$

due to $\Delta < 0$ and $K(x_{4,5}) < 0$. Since the real part of the eigenvalues are less than zero, we conclude that (x_4, y_4) and (x_5, y_5) are stable focus points.

(d) Strong damping: When $\xi^2 + 4K(x_{4,5}) > 0$, for the equilibria (x_4, y_4) and (x_5, y_5) , there exist two unequal real roots

$$\Lambda_{1,2} = \frac{-\xi \pm \sqrt{\xi^2 + 4K(x_{1,2,3})}}{2}$$

due to $\Delta > 0$ and $K(x_{4,5}) < 0$. Since two eigenvalues are less than zero, we conclude that (x_4, y_4) and (x_5, y_5) are stable node points.

(e) Critical damping: When $\xi^2 + 4K(x_{4,5}) = 0$, for the equilibria (x_4, y_4) and (x_5, y_5) , there exist two equal real roots

$$\Lambda_{1,2} = -\frac{\xi}{2}$$

due to $\Delta = 0$ and $K(x_{4,5}) < 0$. It is concluded that (x_4, y_4) and (x_5, y_5) are stable degenerate nodes.

References

1. Parks, H.V., Faller, J.E.: Simple pendulum determination of the gravitational constant. *Phys. Rev. Lett.* **105**, 110801 (2010)

2. Albert Luo, C.J.: *Resonance and Bifurcation to Chaos in Pendulum*. Higher Education Press, Beijing (2017)

3. D’Humières, D., Beasley, M.R., Huberman, B.A., Libchaber, A.: Chaotic states and routes to chaos in the forced pendulum. *Phys. Rev. A* **26**(6), 3483–3496 (1982)

4. Zayas, V.A., Low, S.S., Mahin, S.A.: A simple pendulum technique for achieving seismic isolation. *Earthq. Spectra* **6**, 317–333 (1990)

5. Kim, Y., Kim, S.H., Kwak, Y.K.: Dynamic analysis of a non-holonomic two-wheeled inverted pendulum robot. *J. Intell. Robot. Syst.* **44**, 25–46 (2005)

6. Whitaker, R.: Types of two-dimensional pendulums and their uses in education. *Sci. Educat.* **13**, 401–415 (2004)

7. Farrugia, A.: The regulatory pendulum in transfusion medicine. *Transf. Med. Rev.* **16**, 273–282 (2002)

8. Awrejcewicz, J., Kudra, G.: Modeling, numerical analysis and application of triple physical pendulum with rigid limiters of motion. *Arch. Appl. Mech.* **74**, 746–753 (2005)

9. Awrejcewicz, J., Sendkowski, D., Kazmierczak, M.: Geometrical approach to the swinging pendulum dynamics. *Comput. Struct.* **84**, 1577–1583 (2006)

10. Xu, X., Wiercigroch, M.: Approximate analytical solutions for oscillatory and rotational motion of a parametric pendulum. *Nonlinear Dyn.* **47**, 311–420 (2007)

11. Das, S., Wahi, P.: Initiation and directional control of period-1 rotation for a parametric pendulum. *Proc. R. Soc. A* **472**, 20160719 (2016)

12. Zhang, H., Ma, T.: Iterative harmonic balance for period-one rotating solution of parametric pendulum. *Nonlinear Dyn.* **70**, 2433–2444 (2012)

13. Awrejcewicz, J., Kudra, G., Wasilewski, G.: Chaotic zones in triple pendulum dynamics observed experimentally and numerically. *Appl. Mech. Mater.* **9**, 1–17 (2008)

14. Kazmierczak, M., Kudra, G., Awrejcewicz, J., et al.: Mathematical modelling, numerical simulations and experimental verification of bifurcation dynamics of a pendulum driven by a dc motor. *Eur. J. Phys.* **36**(5), 13 (2015)

15. Ji, J.C., Chen, Y.S.: Bifurcation in a parametrically excited two-degree-of-freedom nonlinear oscillating system with 1:2 internal resonance. *Appl. Math. Mech.* **20**, 350–359 (1999)

16. Krasilnikov, P., Gurina, T., Svetlova, V.: Bifurcation study of a chaotic model variable-length pendulum on a vibrating base. *Int. J. Non-Linear Mech.* **105**, 88–98 (2018)

17. Albert Luo, C.J., Min, F.H.: The chaotic synchronization of a controlled pendulum with a periodically forced, damped Duffing oscillator. *Commun. Nonlinear Sci. Numer. Simulat.* **16**, 4704–4717 (2011)

18. Leven, R.W., Koch, B.P.: Chaotic behaviour of a parametrically excited damped pendulum. *Phys. Lett. A* **86**, 71–74 (1981)

19. Stachowiak, T., Okada, T.: A numerical analysis of chaos in the double pendulum. *Chaos Solitons Fract.* **29**, 417–422 (2006)

20. Kapitaniak, M., Czolczynski, K., Perlikowski, P., Kapitaniak, T.: Synchronization of clocks. *Phys. Rep.* **517**, 1–69 (2012)

21. Najdecka, A., Kapitaniak, T., Wiercigroch, M.: Synchronous rotational motion of parametric pendulums. *Int. J. Non-Linear Mech.* **70**, 84–94 (2015)

22. Yang, C.C.: Synchronizations of rotating pendulums via self-learning terminal sliding-mode control subject to input nonlinearity. *Nonlinear Dyn.* **72**(3), 695–705 (2013)
23. Wojna, M., Wijata, A., Wasilewski, G., Awrejcewicz, J.: Numerical and experimental study of a double physical pendulum with magnetic interaction. *J. Sound Vib.* **430**, 214–230 (2018)
24. Nana, B., Yamgoué, S.B., Tchitnga, R., Wofo, P.: Dynamics of a pendulum driven by a DC motor and magnetically controlled. *Chaos Solitons Fract.* **104**, 18–27 (2017)
25. Awrejcewicz, J., Kudra, G., Wasilewski, G.: Experimental and numerical investigation of chaotic regions in the triple physical pendulum. *Nonlinear Dyn.* **50**(4), 755–766 (2007)
26. Olejnik, P., Awrejcewicz, J.: Coupled oscillators in identification of nonlinear damping of a real parametric pendulum. *Mech. Syst. Signal Process.* **98**, 91–107 (2018)
27. Anh, N.D., Matsuhisa, H., Viet, L.D., Yasuda, M.: Vibration control of an inverted pendulum type structure by passive mass–spring–pendulum dynamic vibration absorber. *J. Sound Vib.* **307**(1–2), 187–201 (2007)
28. Wu, S.T., Siao, P.S.: Auto-tuning of a two-degree-of-freedom rotational pendulum absorber. *J. Sound Vib.* **331**, 3020–3034 (2012)
29. Mahmoudkhani, S.: Improving the performance of auto-parametric pendulum absorbers by means of a flexural beam. *J. Sound Vib.* **425**, 102–123 (2018)
30. Han, N., Cao, Q.J.: Global bifurcations of a rotating pendulum with irrational nonlinearity. *Commun. Nonlinear Sci. Numer. Simulat.* **36**, 431–445 (2016)
31. Ueda, Y.: Randomly transitional phenomena in the system governed by Duffing’s equation. *J. Stat. Phys.* **20**, 181–196 (1979)
32. Lorenz, E.N.: Deterministic nonperiodic flow. *J. Atmos. Sci.* **20**, 130–141 (2004)
33. Gleick, J., Hilborn, R.C.: Chaos, making a new science. *Phys. Today* **56**, 79 (1998)
34. Yorke, L.J.A.: Period three implies chaos. *Am. Math. Mon.* **82**(10), 985–992 (1975)
35. Melnikov, V.K.: On the stability of the center for time-periodic perturbations. *Trans. Moscow. Math.* **12**, 1–57 (1963)
36. Awrejcewicz, J., Holicke, M.M.: Smooth and nonsmooth high dimensional chaos and the Melnikov-type methods. World Scientific, Singapore (2007)
37. Battelli, F., Palmer, K.J.: Chaos in the duffing equation. *J. Differ. Equ.* **101**, 276–301 (1993)
38. Hou, L., Su, X.C., Chen, Y.S.: Bifurcation modes of periodic solution in a Duffing system under constant force as well as harmonic excitation. *Int. J. Bifurcat. Chaos* **29**(13), 1950173 (2019)
39. Guckenheimer, J., Holmes, P.: *Nonlinear Oscillations, Dynamical Systems, and Bifurcations of Vector Fields*. Springer, New York (1983)
40. Kwekt, K.H., Li, J.B.: Chaotic dynamics and subharmonic bifurcations in a non-linear system. *Int. J. Non-Linear Mech.* **31**(3), 277–295 (1996)
41. Awrejcewicz, J., Holicke, M.: Analytical prediction of stick-slip chaos in a double self-excited Duffing-type oscillator. *Math. Probl. Eng.* **834**(6), 369–376 (2006)
42. Cao, Q.J., Wiercigroch, M., Pavlovskaja, E.E., Grebogi, C., Thompson, J.M.T.: Piecewise linear approach to an archetypal oscillator for smooth and discontinuous dynamics. *Philos. Trans. R. Soc. A* **366**, 635–652 (2008)
43. Cao, Q.J., Wiercigroch, M., Pavlovskaja, E.E., Grebogi, C., Thompson, J.M.T.: Archetypal oscillator for smooth and discontinuous dynamics. *Phys. Rev. E* **74**, 046218 (2006)
44. Zhang, W., Yao, M.H., Zhang, J.H.: Using the extended Melnikov method to study the multi-pulse global bifurcations and chaos of a cantilever beam. *J. Sound Vib.* **319**(1–2), 541–569 (2009)
45. Han, Y.W., Cao, Q.J., Chen, Y.S., Wiercigroch, M.: A novel smooth and discontinuous oscillator with strong irrational nonlinearities. *Sci. China-Phys. Mech. Astron.* **55**, 1832–1843 (2012)
46. Feng, J.J., Zhang, Q.C., Wang, W.: Chaos of several typical asymmetric systems. *Chaos Solitons Fract.* **45**, 950–958 (2012)
47. Tian, R.L., Wu, Q.L., Xiong, Y.P., Yang, X.W.: Bifurcations and chaotic thresholds for the spring-pendulum oscillator with irrational and fractional nonlinear restoring forces. *Eur. Phys. J. Plus* **129**, 85–223 (2014)
48. Zhang, X., Zhou, L.Q.: Melnikov’s method for chaos of the nanoplate postulating nonlinear foundation. *Appl. Math. Model.* **61**, 744–749 (2018)
49. Ren, H.P., Zhou, Z.X., Grebogi, C.: Nonlinear dynamics in the flexible shaft rotating-lifting system of silicon crystal puller using Czochralski method. *Nonlinear Dyn.* **1–14**, 771 (2020)
50. Nusse, H.E., Yorke, A.Y.: *Dynamics Numerical Explorations*. Springer, New York (1997)
51. Tian, R.L., Yang, X.W., Cao, Q.J., Wu, Q.L.: Bifurcations and chaotic threshold for a nonlinear system with an irrational restoring force. *Chin. Phys. B* **2**, 136–147 (2012)
52. Hou, L., Chen, Y.S., Fu, Y.Q., Chen, H.Z., Lu, Z.S.: Application of the HB–AFT method to the primary resonance analysis of a dual-rotor system. *Nonlinear Dyn.* **88**(4), 2531–2551 (2017)
53. Zhao, X., Chen, B., Li, Y.: Forced vibration analysis of Timoshenko double-beam system under compressive axial load by means of Green’s functions. *J. Sound Vib.* **464**, 115001 (2020)
54. Hao, Z.F., Cao, Q.J.: The isolation characteristics of an archetypal dynamical model with stable-quasi-zero-stiffness. *J. Sound Vib.* **340**, 61–79 (2015)
55. Sun, X.T., Wang, F., Xu, J.: Dynamics and realization of a feedback-controlled nonlinear isolator with variable time delay. *J. Vib. Acoust.* **141**(2), 021005 (2018)
56. Wiercigroch, M., Najdecka, A., Vaziri, V.: *Nonlinear Dynamics of Pendulums System for Energy Harvesting*. In: *Vibration Problems ICOVP*. Springer, Netherlands (2011)

Publisher’s Note Springer Nature remains neutral with regard to jurisdictional claims in published maps and institutional affiliations.

Terms and Conditions

Springer Nature journal content, brought to you courtesy of Springer Nature Customer Service Center GmbH (“Springer Nature”). Springer Nature supports a reasonable amount of sharing of research papers by authors, subscribers and authorised users (“Users”), for small-scale personal, non-commercial use provided that all copyright, trade and service marks and other proprietary notices are maintained. By accessing, sharing, receiving or otherwise using the Springer Nature journal content you agree to these terms of use (“Terms”). For these purposes, Springer Nature considers academic use (by researchers and students) to be non-commercial.

These Terms are supplementary and will apply in addition to any applicable website terms and conditions, a relevant site licence or a personal subscription. These Terms will prevail over any conflict or ambiguity with regards to the relevant terms, a site licence or a personal subscription (to the extent of the conflict or ambiguity only). For Creative Commons-licensed articles, the terms of the Creative Commons license used will apply.

We collect and use personal data to provide access to the Springer Nature journal content. We may also use these personal data internally within ResearchGate and Springer Nature and as agreed share it, in an anonymised way, for purposes of tracking, analysis and reporting. We will not otherwise disclose your personal data outside the ResearchGate or the Springer Nature group of companies unless we have your permission as detailed in the Privacy Policy.

While Users may use the Springer Nature journal content for small scale, personal non-commercial use, it is important to note that Users may not:

1. use such content for the purpose of providing other users with access on a regular or large scale basis or as a means to circumvent access control;
2. use such content where to do so would be considered a criminal or statutory offence in any jurisdiction, or gives rise to civil liability, or is otherwise unlawful;
3. falsely or misleadingly imply or suggest endorsement, approval, sponsorship, or association unless explicitly agreed to by Springer Nature in writing;
4. use bots or other automated methods to access the content or redirect messages
5. override any security feature or exclusionary protocol; or
6. share the content in order to create substitute for Springer Nature products or services or a systematic database of Springer Nature journal content.

In line with the restriction against commercial use, Springer Nature does not permit the creation of a product or service that creates revenue, royalties, rent or income from our content or its inclusion as part of a paid for service or for other commercial gain. Springer Nature journal content cannot be used for inter-library loans and librarians may not upload Springer Nature journal content on a large scale into their, or any other, institutional repository.

These terms of use are reviewed regularly and may be amended at any time. Springer Nature is not obligated to publish any information or content on this website and may remove it or features or functionality at our sole discretion, at any time with or without notice. Springer Nature may revoke this licence to you at any time and remove access to any copies of the Springer Nature journal content which have been saved.

To the fullest extent permitted by law, Springer Nature makes no warranties, representations or guarantees to Users, either express or implied with respect to the Springer nature journal content and all parties disclaim and waive any implied warranties or warranties imposed by law, including merchantability or fitness for any particular purpose.

Please note that these rights do not automatically extend to content, data or other material published by Springer Nature that may be licensed from third parties.

If you would like to use or distribute our Springer Nature journal content to a wider audience or on a regular basis or in any other manner not expressly permitted by these Terms, please contact Springer Nature at

onlineservice@springernature.com